International Journal of Biological Macromolecules 306 (2025) 141440

Contents lists available at ScienceDirect

International Journal of Biological Macromolecules

journal homepage: www.elsevier.com/locate/ijbiomac

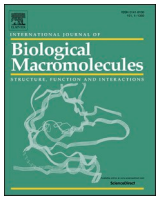

Biomimetic 3D bioprinted bilayer GelMA scaffolds for the delivery of BMP-2 and VEGF exogenous growth factors to promote vascularized bone regeneration in a calvarial defect model in vivo

Emine Alarcin [a,*], Zeynep Puren Akguner [b], Ayca Bal Ozturk [b,c], Gokcen Yasayan [d], Esra Ilhan-Ayisigi [e], Aslihan Kazan [f], Ozlem Yesil-Celiktas [g], Dila Sener Akcora [h], Dilek Akakin [h], Banu Kocaaga [i], Gamze Eren [j], Kasım Gunes [h,k], Oya Kerimoglu [a], Hatice Kubra Seki [d,l], F. Seniha Guner [i,m]

[a] Department of Pharmaceutical Technology, Faculty of Pharmacy, Marmara University, 34668, Istanbul, Türkiye
[b] Department of Stem Cell and Tissue Engineering, Institute of Health Sciences, Istinye University, Istanbul, Türkiye
[c] Department of Analytical Chemistry, Faculty of Pharmacy, Istinye University, Zeytinburnu, Türkiye
[d] Department of Pharmaceutical Technology, Faculty of Pharmacy, Yeditepe University, 34755, Istanbul, Türkiye
[e] Department of Genetic and Bioengineering, Faculty of Engineering and Architecture, Kirsehir Ahi Evran University, Kirsehir, Türkiye
[f] Department of Bioengineering, Faculty of Engineering and Natural Sciences, Bursa Technical University, Bursa, Türkiye
[g] Department of Bioengineering, Faculty of Engineering, Ege University, 35100, Izmir, Türkiye
[h] School of Medicine, Department of Histology and Embryology, Marmara University, 34854, Istanbul, Türkiye
[i] Department of Chemical Engineering, Istanbul Technical University, Maslak, 34469, İstanbul, Türkiye
[j] Private Clinic, Kadıköy, Türkiye
[k] Department of Histology and Embryology, Faculty of Medicine, Sakarya University, Sakarya, Türkiye
[l] Institute of Health Sciences, Marmara University, Istanbul, Türkiye
[m] Sabancı University Nanotechnology Research and Application Center (SUNUM), Sabancı University, 34956, Istanbul, Türkiye

ARTICLE INFO

Keywords:
Controlled growth factor release
3D bioprinting
Bone scaffold
Bilayer scaffold
Vascularization
Bone regeneration

ABSTRACT

The effective treatment of critical-sized bone defects requires a coordinated interaction between osteogenesis and angiogenesis. Inspired by natural bone tissue, we developed a bilayer vascularized bone construct using extrusion-based dual 3D bioprinting. The construct consists of two layers: a bone-mimetic layer, which includes highly methacrylated gelatin ($GelMA_{HIGH}$), hyaluronic acid, alginate, osteoblast cells, and bone morphogenetic protein-2 (BMP-2) loaded polylactic-*co*-glycolic acid (PLGA) nanoparticles; and a vessel-mimetic layer, composed of low methacrylated gelatin ($GelMA_{LOW}$), alginate, endothelial cells, and vascular endothelial growth factor (VEGF)-loaded PLGA nanoparticles. These layers were designed to form hierarchical microstructures that enable sustained release of growth factor (GF) thereby stimulating both osteogenic and angiogenic processes. The nanoparticles were synthesized using a microfluidic platform, achieving a narrow size distribution. The hydrogel bioinks were systematically optimized for printability, and it was found that incorporation of nanoparticles improved their mechanical properties, surface roughness, degradability, and GF release profiles. Notably, GF release followed zero-order kinetics, ensuring consistent delivery over time. The bilayer scaffolds demonstrated superior cell proliferation and spreading compared to single-layer scaffolds, and in vivo experiments showed enhanced repair of calvarial bone defects. These findings highlight the significant clinical potential of bilayer scaffolds with sequential GF delivery for treating critical-sized bone defects.

1. Introduction

The repair of large bone defects caused by severe conditions such as cancers, congenital malformations, fractures, and infections remains a significant clinical challenge [1–3]. Although bone tissue has a remarkable ability to regenerate, its healing is often hindered when the

* Corresponding author at: Marmara University, Faculty of Pharmacy, Department of Pharmaceutical Technology, 34854, Istanbul, Türkiye.
E-mail address: emine.alarcin@marmara.edu.tr (E. Alarcin).

https://doi.org/10.1016/j.ijbiomac.2025.141440
Received 26 March 2024; Received in revised form 15 February 2025; Accepted 23 February 2025
Available online 25 February 2025

damage exceeds a critical size or occurs under pathological conditions [4]. Current bone regeneration techniques, including autologous and allogeneic bone grafting, face limitations such as the need for additional surgeries, complications in bone harvesting, diminished osteoinductive properties, and immune rejection risks [5,6].

To date, a range of advanced strategies has been proposed to enhance the natural regenerative capacity of bone tissue. These approaches commonly involve the use of scaffolds fabricated from synthetic or biomimetic materials, often combined with bioactive molecules or therapeutic cells. By integrating the synergistic effects of structural support with biological stimulation, these methods aim to facilitate osteogenesis and accelerate the healing process, addressing the critical challenges associated with bone repair and regeneration [7,8]. However, many of them fail in promoting effective bone healing due to inadequate early vascularization. Vascularization is crucial for nutrient, oxygen, mineral, and growth factor (GF) transfer during bone regeneration, and insufficient vascular support can delay or impair bone formation [9–11]. Vascular endothelial growth factor (VEGF) plays a critical role in angiogenesis and indirectly supports osteogenesis. Also, it is vital for bone regeneration, providing the mobilization, strengthening, survival, and proliferation of progenitor cells by inducing angiogenesis [9,12,13]. Bone morphogenetic protein-2 (BMP-2) is key for bone induction and is approved by the Food and Drug Administration (FDA) for bone regeneration applications and non-union in humans [14–16]. Co-delivery of these GFs with controllable release kinetics may be an indispensable approach to enhance osteogenesis with angiogenesis required for regeneration. Studies have demonstrated that co-delivery of VEGF and BMP-2 produces synergistic effects, enhancing both angiogenesis and osteogenesis more effectively than BMP-2 alone [17–19]. However, the use of exogenous GFs like BMP-2 and VEGF in bone scaffolds presents some challenges, such as short half-life in physiological conditions, and the need of high doses which increases cost and the risk of side effect [20,21]. A potential solution involves encapsulation of GFs into nanoparticles (NP_{GFs}) to enable controlled release of GFs at lower doses [22]. Microfluidic technology has demonstrated significant advantages over conventional methods, including precise control over particle size and distribution, as well as scalability, and reproducibility [23,24]. Among the polymers approved by FDA and European Medicines Agency (EMA), polylactic-*co*-glycolic acid (PLGA) stands out as an ideal candidate for bone regeneration due to its excellent biocompatibility, biodegradability, versatility, and tunable properties [25].

3D bioprinting has emerged as promising approach for personalized, patient-specific bone defect treatment due to its capacity to create complex 3D structures tailored precisely to the characteristics of bone damage. 3D bioprinting enables the precise layering of biomaterials, GFs, and cells to create scaffolds with a porous structure in order to supports cell adhesion, migration, and vascular network formation. This architecture is essential for oxygen and nutrient delivery, mimicking native tissue microenvironment, and ultimately enhancing bone healing [26–28]. The main challenge of 3D bioprinting is the development of cell-favorable bioinks that have high printability, optimal rheology, post-printing shape fidelity, mechanical stability, and biocompatibility [29].

Among number of bioprinting materials, gelatin methacryloyl (GelMA) is a widely used in bone regeneration due to its tunable mechanical and chemical characteristics. Its structure closely mimics the native extracellular matrix, featuring cell-attaching and matrix metalloproteinase responsive peptide motifs in its structure. However, GelMA bioinks require high concentrations to print effectively, which can compromise survival of encapsulating cells [30–33]. To address this, GelMA is often blended with other polymers or inorganic materials to improve both printability and cellular compatibility [29,34,35]. Yang et al. developed advanced hybrid biomaterials for bone regeneration, including a hydrogel scaffold integrating pearl powder, GelMA, and VEGF for controlled release and synergistic osteogenesis and angiogenesis [36]. They also introduced a Janus microcarrier with hyaluronic acid methacryloyl (HAMA) and GelMA hemispheres for sequential VEGF and BMP-2 release, enhanced by magnetic Fe3O4@SiO2 nanoparticles for targeted delivery, demonstrating coordinated in vivo angiogenesis and osteogenesis [37].

Herein, we designed a multifunctional bilayer hydrogel scaffold with osteogenic and angiogenic properties using dual extrusion 3D bioprinting (Fig. 1). PLGA nanoparticles (NPs) were presented to bioink composition for controlled release of GFs. The scaffold's osteogenic layer (Bioink B) contains highly methacrylated gelatin ($GelMA_{HIGH}$), hyaluronic acid (HA), alginate (Alg), BMP-2 loaded NPs (NP_{BMP2}), and osteoblasts to support bone tissue formation. The angiogenic layer (Bioink V), composed of low methacrylated gelatin ($GelMA_{LOW}$), Alg, VEGF-loaded NPs (NP_{VEGF}), and endothelial cells, was designed to promote blood vessel formation, and to indirect support bone regeneration. This dual-layer design enables controlled, localized release of GFs, enhancing bone and blood vessel formation. To replicate the mechanical properties of bone and vascular microenvironments, particularly in terms of surface stiffness and roughness, GelMA was synthesized with two distinct degrees of methacrylation, named as $GelMA_{HIGH}$ and $GelMA_{LOW}$. HA was incorporated into the bone-mimetic layer due to its regulatory effects on cellular behaviors and tissue functions, such as promoting osteogenic cell migration, proliferation, and differentiation [38,39]. BMP-2 and VEGF were encapsulated within NPs (NP_{BMP2} and NP_{VEGF}, respectively) using a nanoprecipitation method in continuous flow mode on a microfluidic platform to allow for controlled GF release. The two bioinks were systematically optimized for printability, stability, and biological compatibility. In vitro cell adhesion and encapsulation studies were conducted to assess the scaffolds, which were subsequently tested in vivo using a mouse calvarial defect model. Bone tissue formation and healing were evaluated through histological and immunohistological analyses, confirming the scaffold's efficacy in supporting new bone tissue formation.

2. Materials and methods

2.1. Materials

PLGA (P2191, Lactide: Glycolide molar ratio 50:50), poloxamer 407 (16758) and acetonitrile were purchased from Sigma-Aldrich. Gelatin Type A (300 g Bloom), methacrylic anhydride (MA) and 2-hydroxy-1-[4-(2-hydroxyethoxy) phenyl]-2-methyl-1- propanone (Irgacure 2959), Alg, HA, VEGF165 from mouse, BMP-2, 3-(Trimethoxysilyl)propyl methacrylate, 4′,6-Diamidino-2-Phenylindole (DAPI) were purchased from Sigma-Aldrich (St. Louis, MO, USA). Recombinant Human/Mouse/Rat BMP-2 Protein, Recombinant Mouse VEGF 164 Protein, Mouse VEGF Quantikine ELISA Kit and BMP-2 Quantikine ELISA Kit were purchased from R&D Systems Inc., Minneapolis, MN, USA. MC3T3-E1 Subclone 4 was purchased from ATCC, Rockville, MD, USA. Low glucose- Dulbecco's Modified Eagle Media (L-DMEM), α-minimum essential medium (α-MEM), Fetal Bovine Serum (FBS), and Penicillin-Streptomycin (P/S) were purchased from GIBCO. Rhodamine-Phalloidin (AlexaFluor 594) dye, Live/Dead stain kit were purchased from Invitrogen. PrestoBlue™ Cell Viability Reagent was obtained from Thermofisher Scientific Paisley, UK. Anti-collagen I and osteocalcin were purchased from Abcam, Cambridge, UK. The Sensitek HRP (Anti-Polyvalent) reagents and DAB were purchased from Scytek, USA. Hydrogen peroxide was obtained from Merck, Germany.

2.2. Synthesis and in vitro characterization of PLGA nanoparticles using a microfluidic platform

2.2.1. Synthesis of PLGA nanoparticles using a microfluidic platform

NPs were fabricated by nanoprecipitation method in continuous flow mode in a microfluidic platform [40]. The metal microfluidic systems (0.25 mm I.D. and 1.00 mm I.D. three lines connected T-crosses from VICI Valco Instruments Co. Inc.) are composed of two different

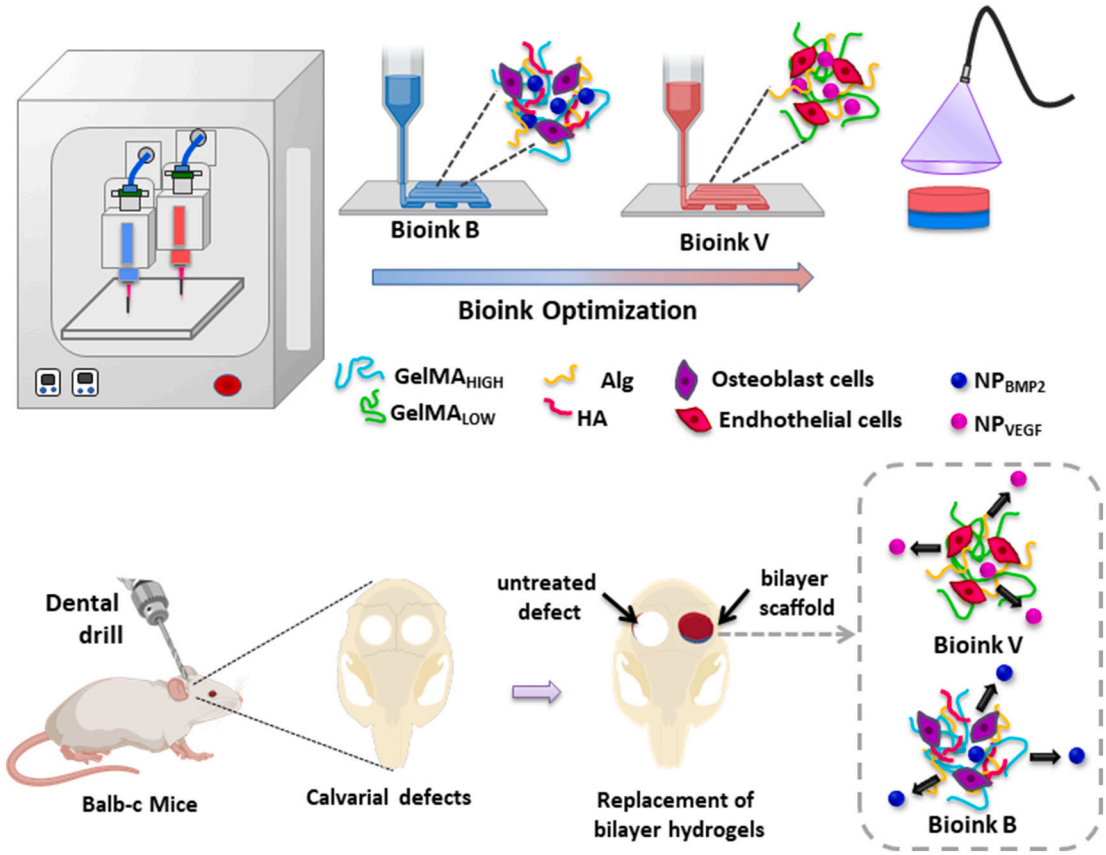

Fig. 1. Schematic showing bioink optimization (top) and calvarial defect model in Balb-C mice (bottom).

microchannels and a micromixer in chip integrated with the syringe pumps. A constant hydrodynamic flux was obtained in all channels by controlling the flow rates of the continuous phase and the disperse phase using a syringe pump. Firstly, GF free NPs were prepared, and key process parameters such as flow rate, channel geometry, polymer concentration and surfactant concentration were optimized. Briefly, PLGA (5 or 10 mg/ml) was dissolved in acetonitrile to form organic phase, which was pumped into the microfluidic platform using syringe pump. Aqueous phase (0.5 % or 1 % (w/v) Poloxamer 407 in distilled water) was introduced into the lateral channels of the T-junction system. The organic phase flow rate was maintained at 10 μL/min, while the aqueous flow rate varied at 50, 100, 200, 400, and 600 μL/min. To evaluate the effect of channel size on particle size distribution, micromixers with two distinct channel diameters (0.25 mm and 1.00 mm I.D.) were used. NP dispersion was collected at the outlet and centrifuged at 13,000 rpm for 20 min. The resulting NPs were washed three times with distilled water to remove any surfactant and GF residues, then lyophilized, dried, and stored at −20 °C. In optimization studies, particle size analysis was performed on at least three randomly selected samples during continuous particle synthesis. For GF loaded NPs, BMP-2 (125 ng/ml, 250 ng/ml or 500 ng/ml as low, medium and high amount, respectively) or VEGF (2.5 μg/ml, 5 μg/ml or 10 μg/ml as low, medium and high amount, respectively) were dissolved in distilled water at various concentrations and mixed with PLGA solution.

2.2.2. *In vitro characterization of nanoparticles*

The mean diameter, PDI and zeta potential of NPs, NP$_{BMP2}$ and NP$_{VEGF}$ were determined by using dynamic light scattering method (Malvern Nano-ZS). Results are given as mean value and ± standard deviation (SD). The surface morphologies of NPs were analyzed by Scanning electron microscopy (SEM) after coating with 10 nm thick gold palladium under vacuum using Leica EM ACE600 sputter-coater. The Fourier-Transform Infrared Spectroscopy (FTIR) (Perkin-Elmer) analysis between the wavelengths of 400–4000 cm^{-1} was performed to determine the functional groups of PLGA and NPs. Differential scanning calorimetry (DSC) was performed to determine the thermal properties of PLGA and NPs. Analyses were carried out with approximately 5 mg of sample at a temperature range of 20–350 °C with a heating rate of 10 °C/min.

The encapsulation efficiency was determined by indirect method. Briefly, during NP production, the supernatant was separated from NPs by centrifugation and the amount of unencapsulated GFs (BMP-2 or VEGF) in aqueous phase was determined by enzyme linked immunosorbent assay (ELISA) method (Biotek EL 800xTM) according to instruction of manufacturers. Encapsulation efficiency was calculated by following formula [41]:

$$\text{Encapsulation Efficiency } (\%) = \frac{(W_1 - W_2)}{W_1} \times 100$$

where W_1 is the total amount GF added initially, and W_2 the amount of unencapsulated free GF in the aqueous phase.

2.3. *Preparation and in vitro characterization of 3D bioprinted scaffolds*

2.3.1. *Synthesis and characterization of gelatin methacrylate*

Considering their mechanical properties, GelMA$_{HIGH}$ and GelMA$_{LOW}$ were synthesized for bone and the vascular layer, respectively. Briefly, 10 % w/v gelatin (type A) was dissolved in Dulbecco's phosphate buffer at 50 °C. Afterwards, 5 ml and 8 ml of methacrylic anhydride were added dropwise to this solution for GelMA$_{LOW}$ and GelMA$_{HIGH}$, respectively, and then stirred at 50 °C for 3 h. In the next step, the reaction was stopped by diluting this solution with Dulbecco's phosphate buffer at 50 °C. The GelMA solution was dialyzed with the dialysis membrane (12–14 kDa cutoff) for 10 days to remove salts and unreacted

methacrylate. The obtained GelMA solution was frozen at 80 °C and lyophilized to form white foam. This GelMA foam was stored at −20 °C. The functional groups of gelatin and GelMA were confirmed by FTIR between the wavelengths of 400–4000 cm^{-1}.

2.3.2. 3D bioprinting set up

A commercial extrusion bioprinter, Axolotl Dual 3D Bioprinter (Axolotl Biosystems, Turkey), was used to print 3D structures. Bioink was loaded into 3 ml print cartridges equipped with 25-gauge blunt needle and the cartridges were placed to the 3D printer. We utilized Slic3r for the adjustment of print settings such as the speed of print-head and extrusion, layer height, infill pattern and density in bioink optimization. Pneumatic pressure was adjusted and 3D models were sliced by Slic3r to create digital patterns for 3D bioprinting. Immediately after bioprinting, the printed structures were treated with 40 s of UV light (360–480 nm) at 3.95 mW/cm^{-2} (OmniCure S2000, Excelitas Technologies, Waltham, MA, USA) for crosslinking to provide shape fidelity.

2.3.3. Bioink preparation

For bone mimetic scaffolds, NP_{BMP2} (2.5, 5 or 10 mg/ml) were dispersed in distilled water containing 0.25 % (w/v) photoinitiator. Subsequently, $GelMA_{HIGH}$ (5–20 %), HA (0.5–2 %) and Alg (0.5–4) dissolved in this dispersion at 50 °C using a magnetic stirrer. For vessel mimetic scaffolds, NP_{VEGF} (2.5, 5 or 10 mg/ml) were dispersed in distilled water containing 0.25 % (w/v) photoinitiator. $GelMA_{LOW}$ (5–20 %) and Alg (0.5–4) dissolved in this dispersion at 50 °C using a magnetic stirrer. The obtained bioink composition was loaded into a 3 ml syringe (EFD Syringe Barrel). Table 1 shows the formulation codes for bone mimetic (Bioink B) and vessel mimetic (Bioink V) scaffolds.

2.3.4. Printability

The minimum pneumatic pressure to extrude the bioink through steady fiber flow was determined as extrusion pressure. The printability of different bioinks was evaluated according to forming a continuous, complete and uniform structure after printing using an optical microscope (Olympus SZX7) connected to a digital camera (Olympus C-5060).

2.3.5. Determination of rheological properties

To determine the rheological properties of bioinks, a rheometer (Anton Paar MCR 301) was used with 25 mm diameter parallel-plate geometry and a solvent trap was used to avoid drying. During the analysis, the distance between the plates was determined as 0.9–1 mm. Angular frequency and strain sweep experiments were performed by applying 1 % stress in the frequency range of 1–100 Hz. The storage module (G′) and loss modules (G″) were determined depending on the frequency change. Viscosities of the bioinks were obtained with 25 mm diameter parallel-plate geometry (PP25) at a shear rate range of 0.1–100 rad/s.

2.3.6. Determination of mechanical properties

1 mm thickness and 8 mm diameter circular samples were printed and UV crosslinked. A texture analyzer (TA Instruments, DE, USA) was used to determine mechanical properties of the scaffolds ($n = 3$). Compression tests were conducted at a cross speed of 1 mm s^{-1} and an 80 % strain level. The slope of the linear section corresponding to 0–10 % of the stress-strain curves was calculated as the compression modulus [42].

Table 1
Formulation table for 3D bioprinted scaffolds.[a]

Formulation		$GELMA_{HIGH}$ (wt%)	$GELMA_{LOW}$ (wt%)	HA (wt %)	Alg (wt %)
Bone mimetic scaffolds (Bioink B)	B7.5	7.5	–	2	0.5
	B10	10	–	2	0.5
	B12.5	12.5	–	2	0.5
	B15.5	15	–	2	0.5
Vessel mimetic scaffolds (Bioink V)	V10	–	10	–	1.5
	V12.5	–	12.5	–	1.5
	V15	–	15	–	1.5

[a] For NP incorporated formulations @2.5NP (2.5 mg/ml NP) or @5NP (5 mg/ml NP) added to these coded.

2.3.7. Swelling studies

The swelling behaviors of scaffolds were assessed in PBS (pH 7.4) at 37 °C for 24 h ($n = 4$) [42]. Briefly, the dry weight of lyophilized scaffolds were recorded and incubated in PBS. At predefined time points, scaffolds were removed from PBS, the excess water was removed from the surface of the scaffolds by using a filter paper and swollen scaffolds weighed. Swelling percentages were evaluated using following formula [42]:

$$\text{Swelling } [\%] = \frac{(W_0 - W_d)}{W_0} \times 100$$

W_0, weight before incubation in PBS, W_d, weight after incubation in PBS for predetermined time points.

2.3.8. Degradation studies

To determine the degradation behaviors of scaffolds, lyophilized scaffolds were weighed and incubated in PBS (pH 7.4) at 37 °C ($n = 3$). At predefined time points, PBS was removed and the scaffolds were rinsed in distilled water. After lyophilization, their dry weights were recorded. After each weighing, scaffolds were placed into PBS again. Weight remaining percentage was calculated using following formula [42]:

$$\text{Weight remaining } [\%] = \frac{(W_0 - W_d)}{W_0} \times 100$$

W_0, dry weight before incubation in PBS, W_d, dry weight after incubation in PBS for predetermined time points.

2.3.9. Scanning electron microscopy (SEM) and atomic force microscopy (AFM)

The surface morphologies of scaffolds were analyzed by SEM after coating with 10 nm thick gold palladium under vacuum using Leica EM ACE600 sputter-coater.

An Ambient AFM™ (Nanomagnetics Instruments) operating in dynamic mode in air was used to obtain topography images of the scaffolds. PPP-NCLR AFM probes (nominal resonance frequency: 190 kHz, nominal force constant: 48 N/m, Nanosensors, Switzerland) were used. Images were obtained using an E-scanner, at scan rates between 0.5 and 3 Hz. Image data was analyzed by an NMI Image Analyzer v1.5 (Nanomagnetics Instruments). The results were obtained by examining a minimum of three different regions of each sample. All images were 5 μm × 5 μm scan. Cross-section analyses and surface roughness calculations were performed using AFM topography image data.

2.3.10. Growth factor release studies

The release of GFs from GF loaded NPs (NP_{BMP2} and NP_{VEGF}), physically entrapped GFs in the hydrogels (B12.5@BMP2 and V12.5@VEGF), and NP loaded hydrogel bioinks (B12.5@5NP_{BMP2} and V12.5@5NP_{VEGF}) were evaluated by the dialysis membrane method. Herein, NP_{BMP2} and NP_{VEGF} were dispersed in dialysis membranes with a certain amount of phosphate buffer saline (PBS, pH 7.4). The prepared dialysis membranes were mixed at 37 ± 0.5 °C and at a constant agitation of 100 rpm. The release medium was collected at predetermined time intervals and the same volume of fresh PBS was added into release medium to provide sink condition. The GF release mechanisms from NPs were determined by the evaluation of zero order, first order, Korsmeyer-Peppas, Higuchi, and Hixson-Crowell kinetic models. The coefficient of determination (r^2) of the first 60 % of drug release was

used to evaluate the optimal model of drug release [43].

2.4. Cell culture

The MC3T3 cells were cultured in α-MEM supplemented with 10 % fetal bovine serum (FBS), 1 % penicillin-streptomycin. The ECs were cultured in low glycose-Dulbecco's Modified Eagle Media (L-DMEM) supplemented with 10 % fetal bovine serum (FBS), 1 % penicillin-streptomycin. Cells were cultured at 37 °C in 5 % CO_2 in a 75 cm^2 culture dish. Cells were passaged when they approached 80–90 % confluency. Cell culture medium was replaced with fresh medium every 2 days.

2.4.1. In vitro cell adhesion studies

In general, MC3T3 cells were seeded at a density 2×10^4 cells/well on B12.5 and B12.5@5NP_{BMP2} hydrogel scaffolds and cultured at 37 °C with 5 % of CO_2. Similarly, ECs were seeded at a density 2×10^4 cells/well on V12.5 and V12.5@5NP_{VEGF} hydrogel scaffolds and cultured at 37 °C with 5 % of CO_2.

Cellular adhesion was evaluated by Rhodamine-Phalloidin and DAPI staining and PrestoBlue assay according to the manufacturer's instructions at days 1, 3, and 7 after cell seeding ($n = 3$).

For Rhodamine-Phalloidin and DAPI staining, hydrogel scaffolds were washed with PBS, fixed with 4 % (w/v) paraformaldehyde for 20 min, permeabilized with 0.05 % (v/v) Triton X-100 for 20 min, and finally blocked with 5 % (w/v) rabbit serum albumin for further 1 h. The samples were incubated in the solution of Rhodamine-Phalloidin for 1 h at 37 °C for F-actin cytoskeleton staining. Afterwards, the samples were incubated in DAPI solution for 30 min at 37 °C for the staining of cell nuclei. Finally, the hydrogel scaffolds were monitored by fluorescence microscopy (Zeiss AxioScope Z1).

For PrestoBlue assay, the cell culture medium was removed and samples were incubated in 10 % (w/v) PrestoBlue in cell culture medium at 37 °C for 1 h, and followed by a microplate reader at 570 nm excitation and 600 nm emission. Samples with no cell seeding were utilized as control, and OD values were normalized to the values of day 0.

2.4.2. In vitro cell encapsulation studies

MC3T3 cells at a density 3×10^6 cells ml^{-1} and ECs at a density 3×10^6 cells ml^{-1} were gently mixed with B12.5 or B12.5@5NP_{BMP2} and V12.5 or V12.5@5NP_{VEGF}, respectively. Then, they were transferred into syringe for bioprinting. Cell encapsulated bioinks were printed and exposed to UV light at a power of 3.95 mW/cm^2 for 40 s to crosslink the structure. Cell encapsulated nanocomposite scaffolds were cultured for a certain time period (1, 3, 7 days) at 37 °C with 5 % CO_2. The culture medium was refreshed every 2 days.

Live/Dead assay was used to evaluate cell viability. After 1, 3, and 7 days of culture, cell encapsulated hydrogels were incubated with calcein-AM (green) and ethidium homodimer-1 (red) for 20 min followed by washing with PBS. The stained hydrogels were evaluated by using an inverted fluorescence microscope. At least six different areas of three samples for each condition were analyzed using ImageJ software, and the cell viability was calculated as the percentage of the number of live cells to total cells ($n = 3$).

Cellular adhesion was determined by Rhodamine-Phalloidin and DAPI staining and PrestoBlue assay according to the manufacturer's instructions at days 1, 3, and 7 of culture.

2.5. In vivo studies

2.5.1. Animals

All animal procedures were carried out under the approval of the Committee of Marmara University Animal Care and Use (approval number of 54.2017.mar). Male BALB/c mice weighting of 25–30 g (7 weeks old) were enrolled in the study. Twenty-four male mice were used in the calvarial bone defect experiment.

2.5.2. Surgical procedure

Surgery was performed under general anesthesia with an intraperitoneal injection of ketamine (50 mg/kg, Ketalar 2 %; Pfizer) and xylazine (10 mg/kg, Alfazyne 2 %, Alfasan). Briefly, an incision was made in the skull skin, the periosteum was carefully removed and the calvaria bone was exposed. A calvarial defect greater than critical-size (5 mm diameter) was created on the center of each side of the calvarial bone using a trephine bur with minimal invasion of the Dura mater [44]. During the procedure, continuous irrigation with PBS was applied to prevent overheating of the edges of the bone and to remove bone debris. After creating defects, mice were randomly divided into 4 groups ($n = 6$ for each group): (*1*) Control (left untreated); (*2*) B12.5@5NP_{BMP2}; (*3*) V12.5@5NP_{VEGF}; (*4*) Bilayer@NP_{GF} (B12.5@5NP_{BMP2}/V12.5@5NP_{VEGF}).

2.5.3. Histology

Samples of calvarial bone were extracted from animals in each group and fixed for 72 h in 10 % neutral formalin. The samples were then decalcified in 10 % ethylenediaminetetraacetic acid (EDTA) 2Na (pH 7.4). The samples were dehydrated in ascending concentrations of ethanol and embedded in paraffin. Sections (5 μm-thick) were cut using a rotary microtome from the paraffin blocks. The sections were stained with hematoxylin and eosin (H&E), Masson's trichrome, and Toluidine blue (TB) stains for histomorphological evaluation. Morphological changes in the bone tissue were examined and photographed using an Olympus DP72 CCD camera attached BX51 photomicroscope (Olympus, Tokyo, Japan) being blinded to the experimental groups.

Neovascularization was scored semiquantitatively as follows: 0 = absent, 1 = minimal capillary, 2 = group of 4–7 capillaries, 3 = broad band of capillaries, and 4 = extensive band of capillaries [45]. The new bone formation was also scored semiquantitatively as 0 = none, 1 = evidence of bone formation, 2 = moderate bone matrix deposited, and 3 = dense highly organized bone matrix [46].

2.5.4. Immunohistochemistry

After decalcification, samples from each group underwent standard tissue processing. Five μm-thick sections were mounted on polylysine-coated slides (Epredia, Netherlands), deparaffinized with xylene, rehydrated with alcohol series, and rinsed with distilled water. For antigen retrieval, sections were microwaved in citrate buffer (pH: 6.0) (Bio-Optica, San Faustino, Italy) and maintained at a temperature below the boiling point. Samples were then cooled to room temperature for 20 min and rinsed in two series of PBS. After 10 min of blocking endogenous peroxidase with 3 % hydrogen peroxide, the sections were rinsed in PBS. Anti-collagen I (COL—I) and osteocalcin (OCN) primary antibodies were applied to the specimens at a dilution of 1:200 for 120 min at room temperature. After washing with PBS, the Sensitek HRP (Anti-Poyvalent) reagents were used according to the manufacturer's instructions. Sections were incubated with biotinylated secondary antibody at room temperature for 20 min prior to washing with PBS. Antibody signals were obtained with DAB incubation as a chromogen. All slides were counterstained with Mayer's hematoxylin and mounted with entellan. Sections were investigated and photographed using a photo-light microscope (DM 750, Leica, Germany; LasV 4.10 program) with an attached camera [47]. Histological evaluation was assessed by two independent observers blind to the study groups, and statistical analysis was performed.

2.6. Statistical analysis

All results are expressed as mean ± standard deviation (SD) of the mean of at least three independent experiments. All statistical analysis was performed by using Prism (GraphPad) software. The statistical significance of the differences between the experimental groups was

analyzed by one-way analysis of variance (ANOVA) with Tukey's Multiple Comparison Test. Histological data was analyzed by ANOVA with Kruskal-Wallis Test. ±95 % confidence interval was used were analysis and P values < 0.05 were reported as statistically significant.

3. Results and discussion

3.1. Preparation and characterization of PLGA nanoparticles

In this study, nanoparticles (NPs) were fabricated using the nanoprecipitation method within a continuous-flow microfluidic platform featuring a multi-inlet mixing unit (Fig. 2A). By introducing PLGA in the organic phase and a surfactant through separate inlet channels, and employing precise flow control for rapid microscale mixing, we achieved reproducible series of NPs with narrow size distributions with high loading capacities. A critical parameter for 3D bioprinting is NP diameter, as this parameter directly influences rheological properties of bioinks and drug release profiles. Microfluidic synthesis enabled precise control over NP sizes due to efficient mixing [48]. Smaller NPs with narrow size distributions facilitated controlled drug release and continuous bioprinting, while larger particles risked clogging the printing needle.

To optimize NP formulation, we initially synthesized GF free NPs to evaluate the effects of various parameters such as channel diameter, polymer and surfactant concentrations, and flow rates, on size and PDI. The results demonstrated that in the micromixer with a larger channel diameter (4D = 1.00 mm) higher lateral flow rates amplified the particle size differences at high and low surfactant concentrations, indicating enhanced control over particle size distribution, particularly at elevated flow rates ($p < 0.05$). At low surfactant concentrations, significantly smaller particles were produced compared to high concentrations. However, this trend was consistently observed only at reduced lateral flow rates (100 and 50 μL) in the micromixer with a narrower channel diameter (0.25 mm) (Fig. 2B and C). Higher polymer/surfactant flow rates also resulted in smaller particle sizes, aligning with previous studies [40]. Channel dimensions and geometry directly affected the particle synthesis and thus the particle size within the microchannel. The mean particle size decreased significantly with the use of thinner

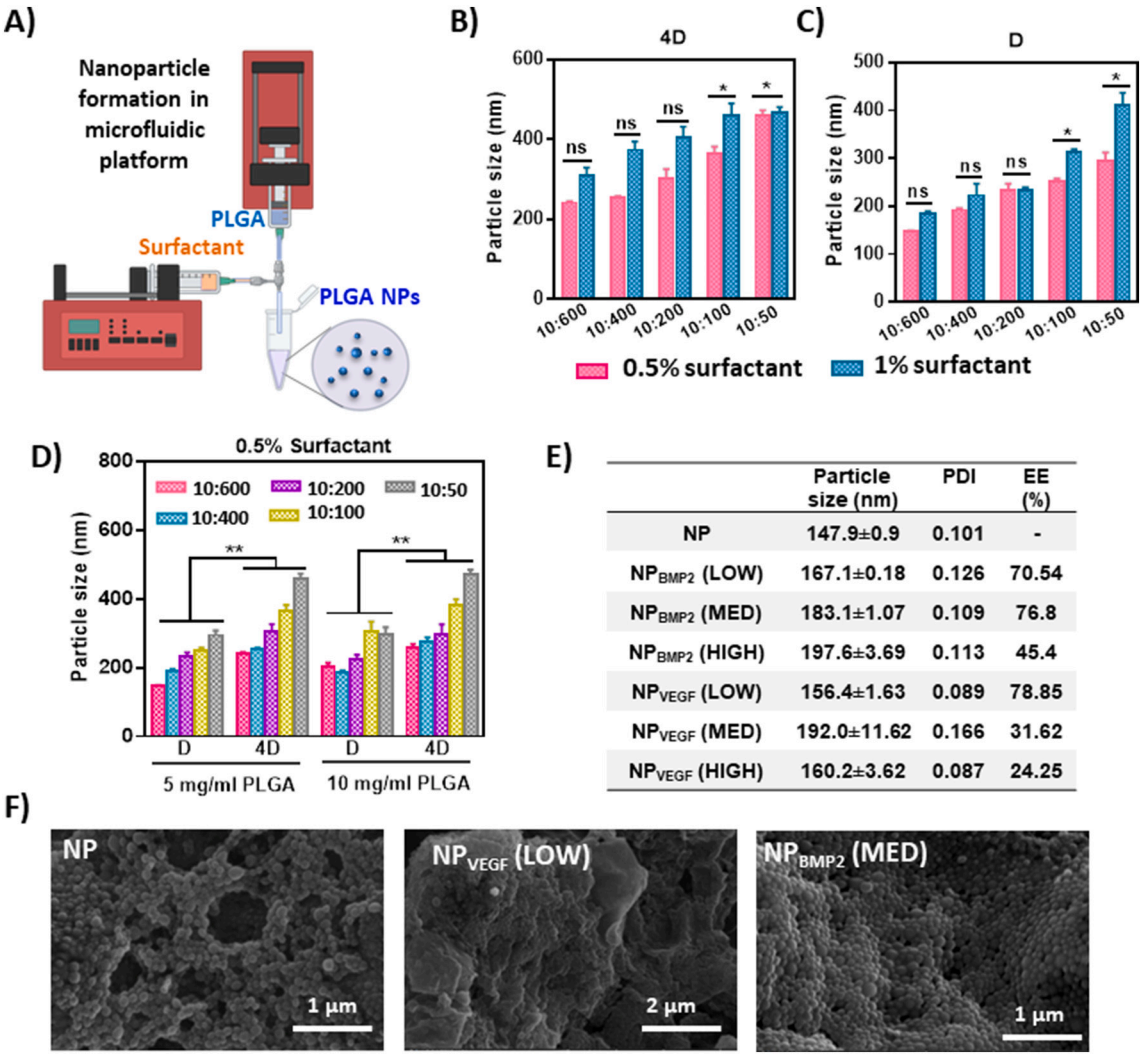

	Particle size (nm)	PDI	EE (%)
NP	147.9±0.9	0.101	-
NP_{BMP2} (LOW)	167.1±0.18	0.126	70.54
NP_{BMP2} (MED)	183.1±1.07	0.109	76.8
NP_{BMP2} (HIGH)	197.6±3.69	0.113	45.4
NP_{VEGF} (LOW)	156.4±1.63	0.089	78.85
NP_{VEGF} (MED)	192.0±11.62	0.166	31.62
NP_{VEGF} (HIGH)	160.2±3.62	0.087	24.25

Fig. 2. (A) Schematic illustration of NP formation in microfluidic platform. (B) Mean sizes of NPs fabricated by using a micromixer with a narrow channel diameter (0.25 mm) under varying surfactant concentrations and polymer/surfactant flow rate. (C) Mean sizes of NPs fabricated by using a micromixer with a higher channel diameter (1 mm) under varying surfactant concentrations and polymer/surfactant flow rate. (D) Comparative analysis of NP sizes fabricated under different polymer concentrations, microchannel diameters, and polymer/surfactant flow rates, represented in a bar graph. (E) Characterization of NPs in terms of particle size, PDI, and encapsulation efficiency for NP_{BMP2} (low, medium, and high BMP-2 concentrations of 125, 250, and 500 ng/ml, respectively) and NP_{VEGF} (low, medium, and high VEGF concentrations of 2.5, 5, and 10 μg/ml, respectively). (F) Representative SEM images NP, NP_{VEGF} (low, 2.5 μg/ml VEGF), and NP_{BMP2} (medium, 125 ng/ml BMP-2) selected for further studies. (ns: $p > 0.05$, *$p < 0.05$, **$p < 0.01$; One-Way ANOVA, Tukey's Multiple Comparison Test.)

channels ($p < 0.01$) for both PLGA concentrations (Fig. 2D). These findings underscore the interplay between channel geometry, surfactant concentration, and flow rate in dictating particle size, highlighting the potential for precise tuning in microfluidic systems. Although polymer concentration is generally reported to influence particle size via its effects on viscosity [49–51], no significant size differences were observed at PLGA concentrations of 5 and 10 mg/ml in our study (Fig. 2D).

The optimal NP formulation was achieved using 5 mg/ml PLGA, 0.5 % (w/v) surfactant, a polymer/surfactant flow rate of 10:600, and a 0.25 mm channel diameter. This yielded NPs with an average size of 147.9 ± 0.9 nm and a PDI of 0.101 ± 0.035 (Fig. 2E). These conditions were subsequently used to encapsulate BMP-2 and VEGF, which slightly increased particle size without compromising PDI values, consistent with literature findings [52]. The zeta potential value of empty NPs was −14.9 ± 5.4 mV, attributable to the carboxylate end groups of PLGA [53]. SEM images confirmed the spherical morphology and smooth surfaces of both NPs and GF-loaded NPs (NP_{BMP2} and NP_{VEGF}). In addition, the obtained particle sizes were quite close to DLS results (Figs. 1F, S1).

FTIR and DSC analyses further characterized the NPs. FTIR spectra of PLGA polymer and NPs are given in Fig. S2A. The characteristic peaks of PLGA were identified through FTIR analysis, including the C═O stretching vibrations of the ester bond at 1747 cm^{-1}, asymmetric and symmetric C-C(=O)-O stretching vibrations within the range of 1269–1165 cm^{-1}, and C—O stretching vibrations between 1165 and 1084 cm^{-1}. Additionally, C—H bending vibrations were observed in the 1450–850 cm^{-1} range. When comparing the FTIR spectra of pure PLGA and NPs, a notable decrease in peak intensity at 2950 cm^{-1} was observed for NPs, suggesting potential structural or compositional modifications in the polymer upon nanoparticle formation. Fig. S2B shows the DSC thermograms of the empty NPs and the PLGA polymer. DSC thermograms showed a shift in the glass transition temperature from 43.7 °C for

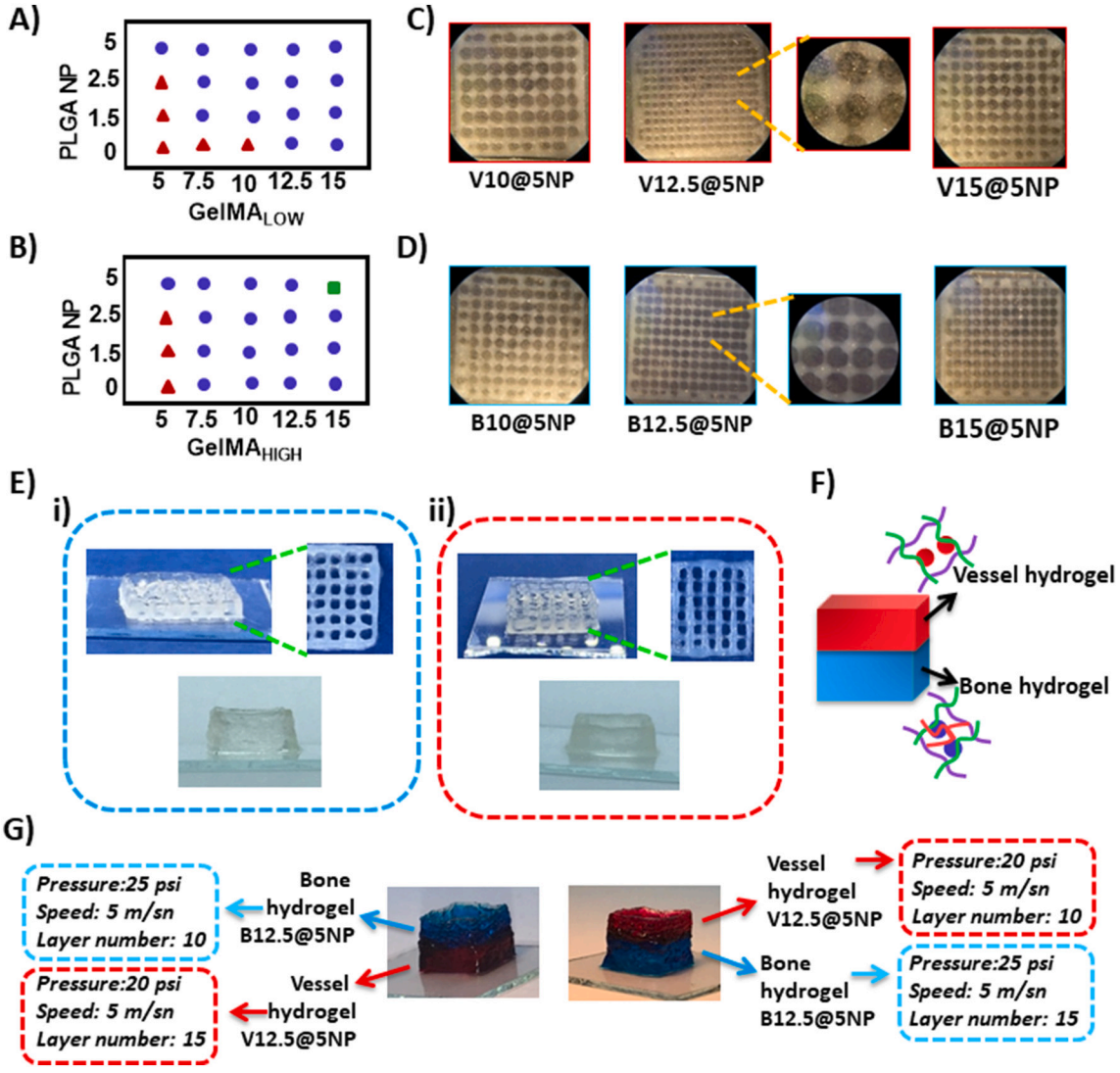

Fig. 3. Printability studies of hydrogel bioinks. (A) Assessment of printability of vessel mimetic bioinks composed of 2 wt% Alg with varying concentrations of $GelMA_{LOW}$ and NPs. (B) Printability evaluation of bone mimetic bioinks composed of 0.5 wt% Alg, 2 wt% HA and varying concentrations of $GelMA_{HIGH}$ and NPs. Symbols indicate printability outcomes: red triangles represent bioinks with insufficient viscosity for printing, blue circles indicate bioinks printable in at least 5 layers, and green squares represent bioinks with excessively high viscosity for printing. (C) Images showing the grid design of vessel mimetic bioinks composed of 2 wt% Alg, 5 mg/ml NPs, and varying $GelMA_{LOW}$ concentrations (V10@5NP, V12.5@5NP and V15@5NP). (D) Images showing the grid design of bone mimetic bioinks composed of 0.5 wt% Alg, 2 wt% HA, 5 mg/ml NPs, and varying $GelMA_{HIGH}$ concentrations (B10@5NP, B12.5@5NP and B15@5NP). (E) Photographs showing the grid and square patterns printed using i) bone mimetic bioink B12.5@5NP and ii) vessel mimetic bioink V12.5@5NP. (F) Schematic representation of bilayer hydrogel composed of bone and vessel mimetic layers (B12.5@5NP/V12.5@5NP). (G) Photographs of the 3D-printed bilayer hydrogel structure (B12.5@5NP/V12.5@5NP).

PLGA to 53.57 °C for NPs, indicating enhanced thermal stability of the synthesized NPs is higher than polymeric PLGA. The endothermic peak around 90–100 °C observed in the NPs is associated with the evaporation of water from the moisture in the sample [54].

The microfluidic platform was crucial for maintaining GF stability and achieving high encapsulation efficiency, outperforming conventional methods where homogenization may compromise GF stability [41]. Encapsulation efficiencies were highest at medium BMP-2 concentrations (250 ng/ml, 76.8 %) and low VEGF concentrations (2.5 μg/ml, 78.85 %) (Fig. 2E). These conditions were selected for subsequent studies to maximize bioavailability while minimizing material waste and associated costs.

3.2. Preparation and in vitro characterization of 3D bioprinted scaffolds

3.2.1. GelMA synthesis and bioink optimization

The functional groups of the synthesized GelMA were confirmed through FTIR analysis, which revealed characteristic amide bands associated with the vibrational states of peptide bonds (Fig. S3A). The peak at 1441 cm^{-1}, corresponding to Amide III, is the result of the vibrations of N—H bonds and, to some extent, C—N bonds. Similarly, the peak at 1522 cm^{-1} (Amide II) is attributed to N—H bond vibrations, while the Amide I peak at 1628 cm^{-1} corresponds to C═O bond vibrations. The position and intensity of the Amide I peak reflect the secondary structure of the gelatin. Additionally, the peaks observed at 3260 cm^{-1} and 2915 cm^{-1} are attributed to with O—H and C—H stretching vibrations, respectively. These findings are consistent with previously reported data [55,56], further validating the successful synthesis and structural integrity of GelMA.

Using a dual extrusion bioprinter, we constructed 3D heterogeneous structures based on bone and vessel mimetic bioinks that we designed (Fig. 3). To prepare the bioinks for bilayer vascularized bone scaffolds, we first systematically optimized the bioinks for extrusion from the print head to generate a solid 3D structure. GelMA was selected as the basic bioink material due to its easily tunable and photocrosslinkability, superior biocompatibility and controllable biodegradability [29]. However, extruding GelMA alone proved to be challenging. Previous studies have shown that while GelMA could be printed at high concentrations above 7 wt%, such concentrations may decrease cellular activity due to the rigidity of the crosslinked structure. Hence, it is quite common to print lower concentration of GelMA with other polymers such as Alg [29,57,58].

Herein, we added Alg to bioinks to control the viscosity of bioinks and provide sufficient extrusion. Without the addition of Alg, the viscosity of the bioink was insufficient to build a stable 3D structure after extrusion. We were able to print $GelMA_{LOW}$-Alg bioinks at extrusion pressures between 15 and 25 psi using 27 gauge needles, and $GelMA_{HIGH}$-Alg bioinks at 18–30 psi with the same needle size. In general, increasing GelMA and Alg concentration along with higher methacryloyl substitution resulted in better printability (Fig. S4A and B). To better support bone regeneration and modulate the extrusion of bioink, we added HA to the bone bioink composition, testing two concentrations (0.5 and 2 wt%) of HA to optimized $GelMA_{HIGH}$-Alg bioinks (Fig. S4A). The addition of HA improved the printability and post-printing shape fidelity of the constructs.

To determine the optimal concentration of NPs for enhanced extrusion, we incorporated various concentrations (1.5 mg/ml, 2.5 mg/ml or 5 mg/ml) of NPs into both vasculogenic and osteogenic bioinks. As shown in Fig. 3A and B, the addition of NPs improved the printability and post-printing shape fidelity of the constructs.

Considering printability, mechanical properties, and cellular behavior during 3D cell encapsulation, we selected the following bioink formulations: 12.5 wt% $GelMA_{HIGH}$-2 wt% HA-0.5 wt% Alg bioink containing 5 mg/ml NPs for the osteogenic component (B12.5@5NP), and 12.5 wt% $GelMA_{LOW}$-1.5 wt% Alg bioink containing 5 mg/ml NPs for the vasculogenic component (V12.5@5NP). Afterwards, we printed bilayer vasculogenic bone scaffolds, which were optimized individually as a single layer, using 3D bioprinter (Fig. 3F). The final bilayer scaffolds, composed of B12.5@5NP (osteogenic layer) and V12.5@5NP (vasculogenic layer), consisted of 30 layers in total. The structural integrity of the bilayer constructs was clearly maintained post-printing, demonstrating the effectiveness of the bioink formulations.

3.2.2. Rheology

Bioinks should be extruded smoothly from a nozzle, minimizing shear stress on the encapsulated cells while avoiding physical clogging. Furthermore, they should maintain their shape with high fidelity after printing, facilitated by their shear thinning and self-healing properties [59,60]. To meet these requirements, bioinks need to exhibit stability and possess high viscoelastic properties. Therefore, our study focused on investigating the rheological properties across various primary categories: (i) extrudability and viscoelastic properties were evaluated through strain and frequency sweep analyses, (ii) self-healing property was assessed conducting thixotropic oscillatory strain amplitude sweep measurements, which were performed in six distinct regions, (iii) stability, durability, and recovery abilities were tested through a creep test. By examining these rheological properties, we aimed to understand and enhance the performance of bioinks for effective 3D bioprinting applications.

The frequency sweep analysis indicated that both G' and G'' values show a slight dependence on frequency in the range tested, with G' consistently being greater than G'', suggesting that both bio-inks possessed solid-like viscoelastic structures with strong interconnectivity (Fig. 4A and C). Previously, hydrogels with $G' > G''$ ratio were reported to support increased cell viability in injectable cell therapies. Herein, B12.5 exhibited a higher G' value compared to V12.5. Notably, the inclusion of NPs in the bioinks significantly improved their G' values. This effect was particularly pronounced in B12.5@5NP, which can be attributed to its highly interconnected network structure.

The phase angle, represented by tan δ (tan $\delta = G''/G'$) provides further insight into the bioinks' rheological behavior. In this study, the tan δ values for all formulations ranged between 0.23 and 0.36. Bioinks having tan δ 0.25 to 0.45 were reported to exhibit suitable printability, structural integrity, and extrusion uniformity [61]. Similarly, Indurkar and coworkers observed that bio-inks with tan δ below 0.15 exhibited droplets instead of filaments during printing, while those with tan δ values between 0.151 and 0.209 exhibited filament formation. They suggested that tan $\delta > 0.151$ is ideal for filament formation. It has also been emphasized that the tan δ values suitable for printing may vary according to the bioink formulation [62].

Injectability and extrudability are crucial factors for hydrogels used as bioinks in extrusion-based 3D bioprinting [63]. Under low-strain conditions, the moduli of STHs were unaffected by the strain amplitude. However, after reaching the critical strain point, the moduli decreased sharply as their internal structure was compromised (Fig. 3B and D). Similarly, the results exhibited a linear decrease in the complex viscosity of the samples with frequency on a double logarithmic scale, demonstrating a strong shear-thinning behavior (Fig. 4E). This shear-thinning behavior is responsible for aligning the polymer chains with the flow, thereby contributing to the self-healing and shape-molding properties of the bioprinted structures [64]. The pronounced shear-thinning behavior of the synthesized bioinks can be attributed to the dynamic nature of hydrogen bonding which greatly facilities the extrusion process. This rheological characteristic is vital for any bioink, including cells to be printed using extrusion-based bioprinters. Importantly, with the presence of NPs in bioinks, the shear-thinning behavior was maintained and the viscosity increased (Fig. 4E).

We also evaluated the creep and recovery properties of the bioinks, as these are essential for assessing the stability and durability of the printed constructs. In this study, the bioinks were exposed to constant shear stresses (creep) of 25 Pa for a period of 300 s, and the resulting time-dependent deformation was subsequently evaluated. Following

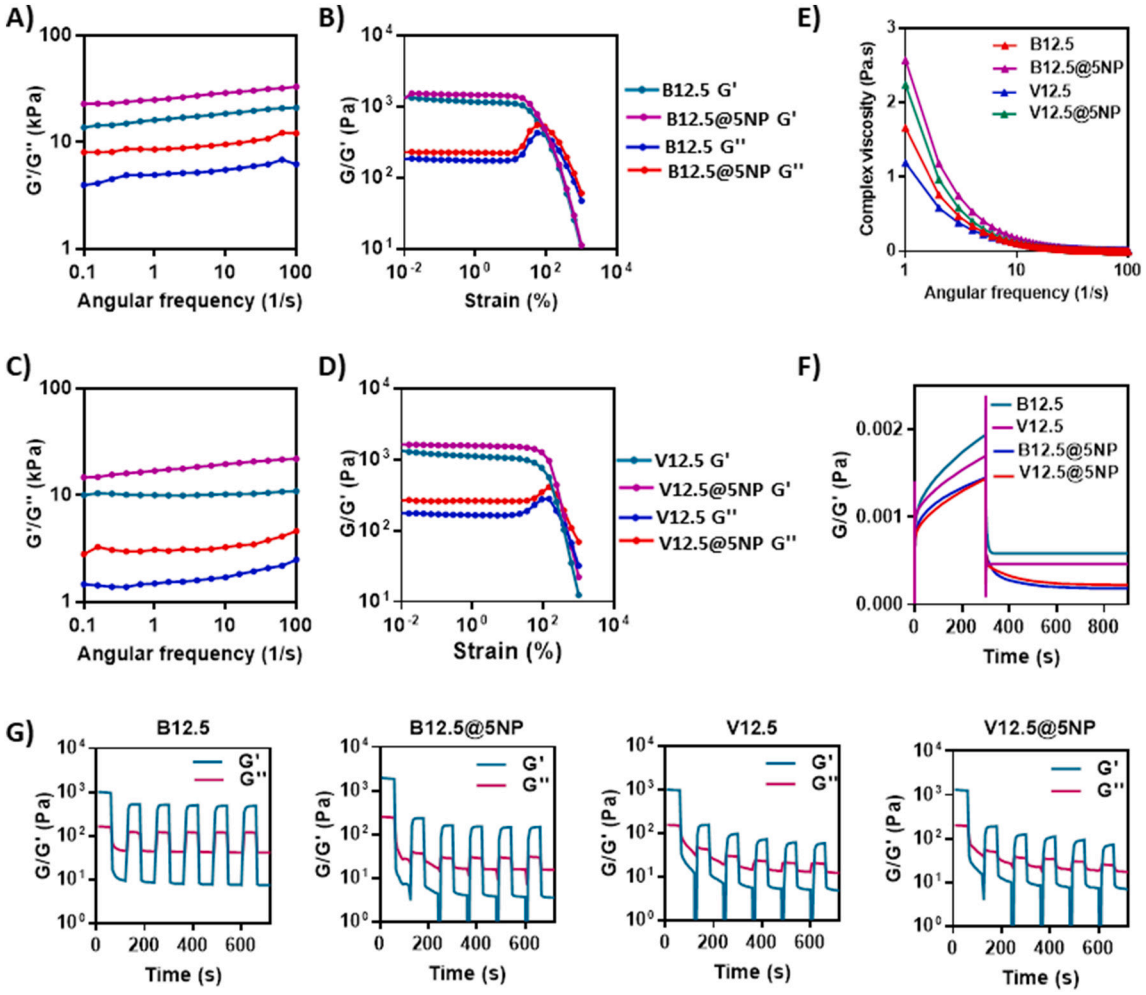

Fig. 4. Rheological properties of hydrogel bioinks. (A) Frequency sweep analysis showing storage modulus (G′) and loss modulus (G″) of Bioink B. (B) Storage modulus and loss modulus of Bioink B as a function of strain. (C) Frequency sweep analysis showing storage modulus (G′) and loss modulus (G″) of Bioink V. (D) Storage modulus and loss modulus of Bioink V as a function of strain. (E) Complex viscosity of bioinks indicating shear thinning behavior of bioinks. (F) The creep recovery of bioinks indicating higher elasticity of bioinks. (G) Six-cycled thixotropic oscillatory strain amplitude sweep measurements indicating that bioinks could recover the damage during the extrusion process.

this, after the stress was released, deformation recovery was recorded for an additional 600 s [65]. The creep recovery values for B12.5 and V12.5 were 73.9 % and 80.7 %, respectively. The bioinks containing NPs exhibited higher creep recovery values (B12.5@5NP: 87.2; V12.5@NP: 84.5), indicating greater elasticity and improved printability of the formulations (Fig. 4F). These findings align with the results obtained from the frequency sweep analysis.

Hydrogel bioinks might be subjected to strain-induced network damage during the extrusion bioprinting [66], maintaining structural stability through self-healing properties is crucial. To mimic the extrusion and self-healing ability, we conducted six-cycled thixotropic oscillatory strain amplitude sweep measurements (Fig. 4G). The high shear strain (1000 %) resulted in a viscous-like structure ($G'' > G'$), indicating gel-sol transition (a flowable structure) of the system. However, upon decreasing the applied strain to a low value (1 %), bioinks (B12.5, B12.5@5NP, V12.5, V12.5@5NP) recovered their initial tan δ values, with a 56.5, 69.2, 68.8, and 46.0 RS%, respectively. These results confirmed that the synthesized bioinks could recover from damage during the extrusion process, making them suitable for high-quality 3D bioprinting.

3.2.3. FTIR studies

The structure of the bioink composition and photocrosslinked hydrogel scaffolds was confirmed using FTIR, which showed the presence of Amid-I, Amid-II, and Amid-III peaks at 1441 cm^{-1}, 1522 cm^{1}, and 1628 cm^{-1}, respectively, in the $GelMA_{LOW}$ and $GelMA_{HIGH}$ samples (Figs. 5A and S3A). Additionally, O—H and C—H stretching vibrations were identified at 3260 cm^{-1} and 2915 cm^{-1}, respectively. For alginate (Alg), characteristic O—H and C—H stretching vibrations were observed within the ranges of 3000–3600 cm^{-1} and 2920–2850 cm^{-1}, respectively (Fig. S3B). The carboxylate salt ion asymmetric and symmetric stretching vibrations were appeared at 1649 and 1460 cm^{-1}, respectively. The bands at 1107 cm^{-1} and 935 cm^{-1} were assigned to the C—O stretching vibrations of the pyranosyl ring and the C-C-H and C-O-H deformations [67]. The IR spectra of HA showed O—H stretching vibrations at 3443 cm^{-1} and carbonyl stretching vibrations corresponding to carboxylic acid and amide groups at 1720 cm^{-1} and 1648 cm^{-1}, respectively (Fig. S3B). Ether bands were observed at 1151 and 1034 cm^{-1} regions [68]. In the FTIR spectra of bone-mimetic hydrogel scaffolds (B12.5 and B12.5@5NP), characteristic peaks of GelMA, HA, and Alg were clearly observed. Similarly, for vessel-mimetic hydrogels (V12.5 and V12.5@5NP), peaks corresponding to GelMA and Alg were detected (Figs. 5A and S3C). Notably, the characteristic peaks of NPs were not discernible in the hydrogel composition, likely due to their low concentration (5 mg/ml).

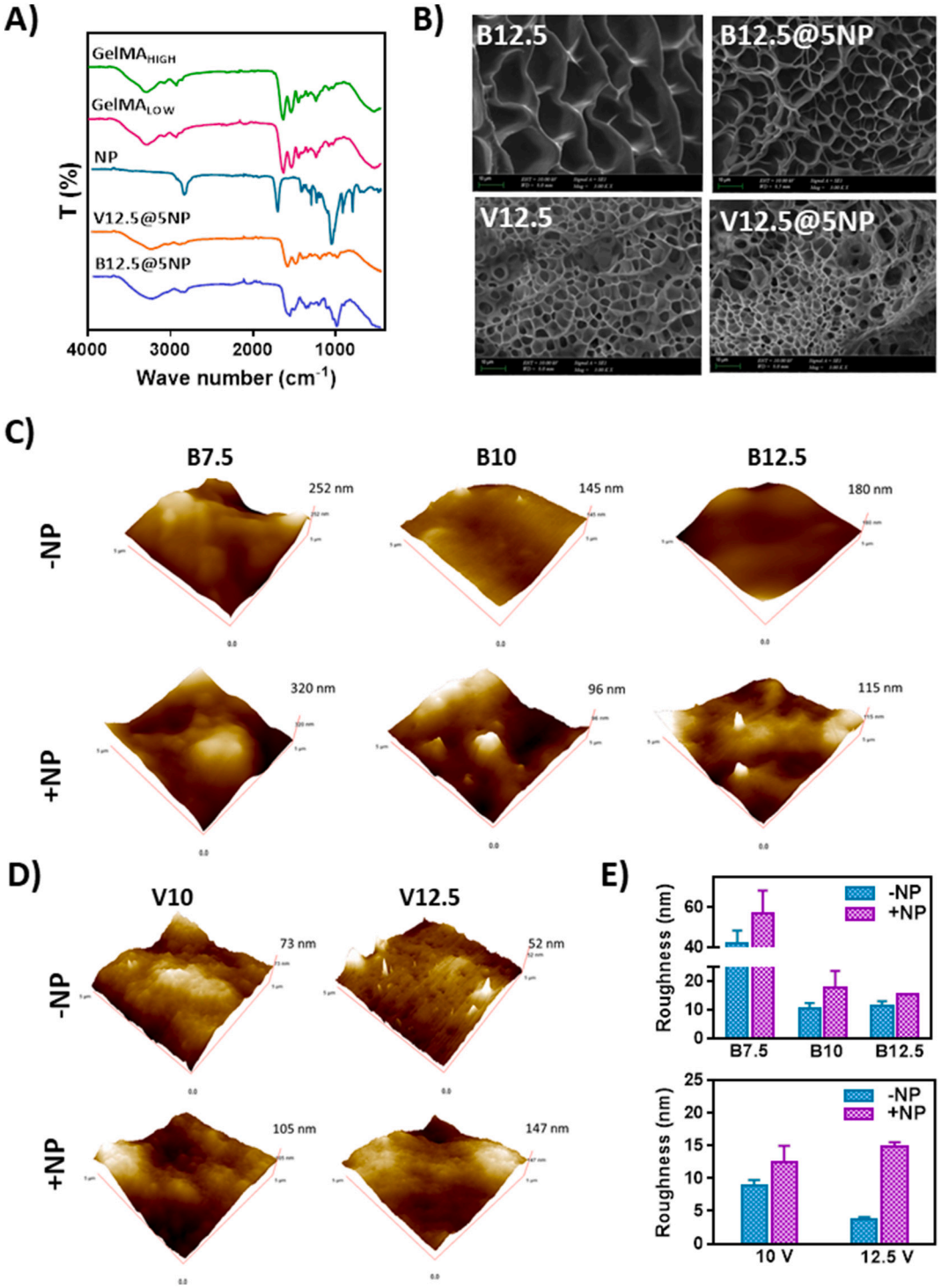

Fig. 5. (A) FTIR spectra of GelMA$_{LOW}$, GelMA$_{HIGH}$, NPs, and composite bioinks V12.5@5NP and B12.5@5NP, highlighting characteristic functional groups and interactions. (B) SEM images of vessel-mimetic (V12.5) and bone-mimetic (B12.5) scaffolds, both with and without 5 mg/ml NPs(@5NP), showcasing morphological differences. (C) Surface topographies for bone-mimetic scaffolds without (B7.5, B10 and B12.5) and with 5 mg/ml NPs (B7.5@5NP, B10@5NP and B12.5@5NP), as well as (D) vessel mimetic scaffolds without (V10 and V12.5) and with 5 mg/ml NPs (V10@5NP and V12.5@5NP). All AFM images were 5 μm × 5 μm scan. (E) Surface roughness values for bone mimetic (top) and vessel mimetic (bottom) scaffolds acquired from AFM image data.

3.2.4. *Surface morphology and topography*

The surface characteristics of bone and vessel mimetic hydrogels were comprehensively evaluated (Figs. 5B, S5 and S6). SEM analysis revealed that all hydrogel scaffolds exhibited a highly porous structure, critical for facilitating cellular activities. Importantly, the presence of NPs did not lead to any particle aggregation in the scaffolds, and NPs uniformly distributed throughout the scaffolds. As the GelMA ratio increased, the pore structures became more regular, further enhancing the scaffold's suitability for tissue engineering applications.

AFM studies provided detailed insights into the surface topography and roughness of the scaffolds. The analysis showed that blending GelMA$_{HIGH}$ with HA, Alg, or a combination of both produced scaffolds with varying surface roughness (Fig. S7). Studies with GelMA$_{HIGH}$ alone could not be performed due to the high adhesion of GelMA$_{HIGH}$ to the AFM

probe [69]. While $GelMA_{HIGH}$/HA exhibited a flatter surface with surface roughness value of 5.7 nm, $GelMA_{HIGH}$/Alg and $GelMA_{HIGH}$/HA/Alg displayed similar topographical features and slightly higher roughness values of 9.7 nm and 10.5 nm, respectively. This smoother topography may reflect enhanced polymer compatibility and homogeneity due to stronger intermolecular interactions.

In bone-mimetic scaffolds, increasing the GelMA concentration significantly reduced surface roughness. This trend is reflected in the measured roughness values: 41.8 nm for B7.5, 10.5 nm for B10, and 11.4 nm for B12.5 (Figs. 5C, E, and S7) Increasing GelMA concentration resulted in smoother surfaces, likely due to enhanced molecular interactions between positively charged GelMA and negatively charged polymers (Alg and HA). This finding aligns with previous studies suggesting that smoother topographies indicate a more homogeneous mixture [70]. The addition of NPs altered the surface properties, creating distinct domains and increasing surface roughness, particularly in GelMA concentration formulations. NP containing scaffolds exhibited higher roughness than their NP free counterparts: 56.6 nm for B7.5@5NP, 17.8 nm for B10@5NP and 15.3 nm for B12.5@5NP (Fig. 5E). These findings highlight the ability to modulate scaffold properties by adjusting GelMA concentration and NP content, enabling tailored designs for specific applications.

Similarly, the analysis of vascular-mimetic hydrogels revealed a dependency on GelMA concentration for surface characteristics (Fig. 5D and E). The lower methacrylation degree and concentration of $GelMA_{LOW}$ in vascular formulations likely contributed to increased adhesiveness, complicating AFM imaging. For instance, topography images could not be obtained for V7.5 due to adhesiveness of the hydrogel sample to the AFM probe. Nonetheless, roughness measurements showed that higher $GelMA_{LOW}$ concentrations (V12.5 with roughness value of 3.8 nm) yielded flatter surfaces compared to lower concentrations (V10 with roughness value of 9 nm), consistent with the behavior observed in bone-mimetic scaffolds (Fig. 5C). The addition of NPs further increased surface roughness, although these changes were less pronounced compared to the bone-mimetic formulations, with roughness values of 12.4 nm and 14.9 nm for V10@5NP and V12.5@5NP, respectively.

In conclusion, this study demonstrates that the interplay between scaffold composition, polymer interactions, and NP incorporation significantly influences the surface and morphological properties of bioink based hydrogels. These results provide valuable insights for optimizing scaffold design to enhance functionality and efficacy for their application in bone and vascular tissue engineering.

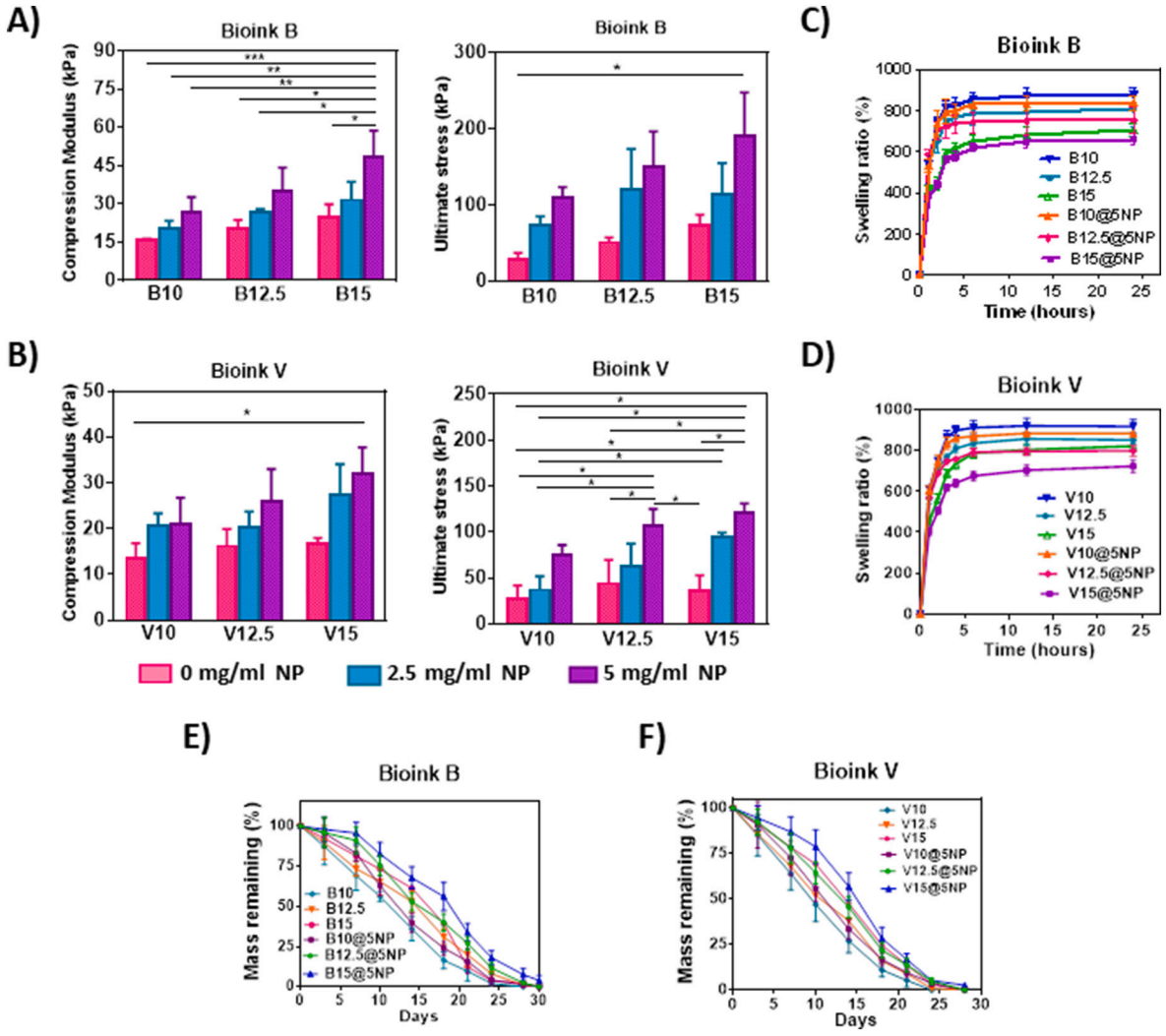

Fig. 6. Evaluation of mechanical properties, swelling behavior, and degradation profiles of bioinks. (A) Compression modulus and ultimate stress at break of bone-mimetic bioinks (B10, B12.5, and B15) with or without NPs (0 mg/ml, 2.5 mg/ml @2.5NP, and 5 mg/ml @5NP). (B) Compression modulus and ultimate stress at break of vessel-mimetic bioinks (V10, V12.5, and V15) with or without NPs (0 mg/ml, 2.5 mg/ml @2.5NP, and 5 mg/ml @5NP). (C) Swelling behavior of bone mimetic bioinks. (D) Swelling behavior of vessel mimetic bioinks. (E) Degradation behavior of bone mimetic bioinks. (F) Degradation behavior of vessel mimetic bioinks. (ns: $p > 0.05$, $*p < 0.05$, $***p < 0.001$; One-Way ANOVA, Tukey's Multiple Comparison Test.)

3.2.5. Mechanical properties

To regulate the activity of OBs and osteogenesis, as well as to influence ECs and angiogenesis, extracellular matrix stiffness plays a crucial role [71,72]. Therefore, the goal of our study was to modulate the stiffness of hydrogel scaffolds. As shown in Fig. 6A and B, our analysis of the mechanical properties revealed that both the compression modulus and ultimate stress at break increased progressively with higher GelMA (for both $GelMA_{HIGH}$ and $GelMA_{LOW}$) and Alg concentrations. These improvements in mechanical properties can be attributed to the increased methacryloyl substitution, which promotes covalent crosslinking and results in a denser scaffold structure.

The primary objective of this study was to design a scaffold incorporating NPs, so we also assessed the mechanical properties of scaffolds containing 2.5 mg/ml or 5 mg/ml NPs. The addition of NPs resulted in a significant and gradual improvement in the compression modulus for all hydrogel formulations. For example, the compression modulus values for B12.5, B12.5@2.5NP, and B12.5@5NP were 20.575 ± 3.14 kPa, 26.701 ± 1.263 kPa, and 34.953 ± 9.242 kPa, respectively (Fig. 6A). Correspondingly, the ultimate stress at break for these formulations increased from 51.071 ± 9.147 kPa for B12.5, to 72.627 ± 12.419 kPa for B12.5@2.5NP, and 109.456 ± 46.707 kPa for B12.5@5NP.

These results align with existing knowledge that OBs prefer stiffer matrices for their growth and proliferation, providing suitable biomechanical conditions for cellular processes such as attachment, spreading, elongation, proliferation, and migration.

Similarly, the compression modulus values for the vascular mimetic formulations, V12.5, V12.5@2.5NP, and V12.5@5NP, were 16.190 ± 3.7 kPa, 20.13 ± 3.586 kPa, and 25.984 ± 7.006 kPa, respectively (Fig. 6B). These values fall within the optimal biomechanical range for endothelial cell activities [73,74]. Additionally, the ultimate stress at break for these formulations was 44.140 ± 25.555 kPa, 63.077 ± 24.206 kPa, and 106.983 ± 18.203 kPa for V12.5, V12.5@2.5NP, and V12.5@5NP, respectively.

Finally, we assessed the mechanical properties of the bilayer hydrogels (Fig. S8). The compression modulus for the B12.5/V12.5 and B12.5@NP/V12.5@NP hydrogels was determined to be 17.191 ± 1.53 kPa and 31.608 ± 8.3 kPa, respectively. Additionally, the ultimate stress at break was measured at 48.264 ± 15.38 kPa for B12.5/V12.5 and 133.47 ± 26.71 kPa for B12.5@NP/V12.5@NP. Importantly, no significant differences were observed in the individual properties of each layer or between the bilayer hydrogels. These findings provide valuable insight into the mechanical performance of the scaffolds, highlighting their potential for bone tissue engineering applications.

3.2.6. Swelling and degradation

Swelling and hydration properties of hydrogels are key factors influencing their diffusion, surface characteristics, mechanical properties, and drug release behavior. These parameters also significantly impact cellular infiltration following in vivo implantation [75–77]. In this study, all types of hydrogels displayed a high swelling rate (>500.0 %), which is advantageous for facilitating the release of entrapped GFs, supporting cell growth, and enabling oxygen transport. Increasing GelMA concentration resulted in a reduced swelling degree, which can be attributed to the stronger covalent bonding that occurred at higher concentrations. All hydrogels reached equilibrium swelling after approximately 6 h of incubation. For the bone mimetic hydrogels, the swelling rates were 804.867 ± 86.541 % (B12.5) and 753.641 ± 61.952 % (B12.5@5NP) for the 0 and 5 mg/ml NP concentrations, respectively (Fig. 6C). Similarly, the vessel mimetic hydrogels showed swelling rates of 851.039 ± 17.843 % (V12.5) and 798.129 ± 25.615 % (V12.5@5NP) for the 0 and 5 mg/ml NP concentrations, respectively (Fig. 6D). The presence of NPs in the hydrogel formulations decreased the swelling rate, as the NPs formed physical interactions with the hydrogel network due to their negative charge, resulting in a more compact structure.

Degradation studies revealed that all photocrosslinked hydrogels exhibited sustained degradation in PBS over a period of up to one month. An increase in GelMA concentration and methacrylation degree resulted in a slower degradation rate, likely due to the enhanced covalent crosslinking. Importantly, the addition of NPs further reduced the degradation rate. Specifically, as the NP concentration increased from 0 to 5 mg/ml, the remaining mass (%) after 7 days of incubation increased from 73.465 % ± 4.623 for B12.5 to 91.672 % ± 8.377 for B12.5@5NP (Fig. 6E). Similarly, for the vessel mimetic hydrogels, the remaining mass (%) increased from 68.546 % ± 6.319 for V12.5 to 77.981 % ± 8.351 for V12.5@5NP (Fig. 6F).

The incorporation of NPs into the hydrogel network resulted in a more compact structure, enhancing the physical interactions between the NPs and the hydrogel matrix, which in turn contributed to the prolonged degradation period. Bone mimetic hydrogels exhibited a longer degradation time compared to vessel mimetic hydrogels, which is advantageous for bone regeneration as it allows for adequate time for angiogenesis to occur [78].

3.2.7. Growth factor release

The use of lower dose dual GFs (BMP-2 and VEGF) plays a pivotal role in promoting the vascularized bone structures. To achieve this, a controlled release system was designed to sequentially deliver BMP-2 and VEGF, leveraging their synergistic effects to enhance bone formation. In our approach, BMP-2 and VEGF were loaded into separate hydrogel layers. We also hypothesized that embedding GF loaded NPs into the hydrogels would enable a more controlled and sustained release of the GFs over an extended period. To evaluate the effect of different GF immobilization methods on the release profiles, we systematically compared the release of GFs from various formulations, including, GF loaded NPs (NP_{BMP2} and NP_{VEGF}), physically entrapped GFs in the hydrogels with no NPs (B12.5@BMP2 and V12.5@VEGF), and NP loaded hydrogel bioinks ($B12.5@5NP_{BMP2}$ and $V12.5@5NP_{VEGF}$) (Fig. 7A).

We first investigated the release rate of GFs from NPs. Consistent with existing literature [41,79], NPs exhibited a biphasic release profile, with an initial burst release followed by a slower release. The initial burst release was attributed to the release of GFs weakly attached to the surface of the NPs and GFs located near the surface of the particle. This initial burst release is essential for providing the initial loading dose. This is then followed by prolonged release of the GFs. BMP-2 release from NP_{BMP2} showed that approximately 20 % of BMP-2 was released after three days (Fig. 7B), with 41.2 % and 55.7 % released by days 7 and 14, respectively, and a cumulative release of 64.9 % at the end of 4 weeks (Fig. 7B). Similarly, VEGF release from NP_{VEGF} showed 29 % release after three days, with 44.6 % and 59.3 % released by days 7 and 14, respectively, reaching 67.16 % at the 4 week mark (Fig. 7C). These release profiles suggest a compatibility with the typical timeframes required for bone healing.

Afterwards, we evaluated the release of physically entrapped GFs in hydrogel matrix (B12.5@BMP2 and V12.5@VEGF). For BMP-2, approximately 61.3 % and 74.6 % of the encapsulated GF was released from B12.5@BMP2 on days 7 and 14, respectively, with nearly 97.2 % released by the end of the 4 week incubation period (Fig. 7B). For VEGF, the release from V12.5@VEGF was faster than from NPVEGF, with 69.4 % and 81.6 % released on days 7 and 14, respectively, and 100 % released by week 4 (Fig. 7C).

We also examined the release of GFs from NP_{GF} entrapped hydrogels ($B12.5@5NP_{BMP2}$ and $V12.5@5NP_{VEGF}$). For BMP-2 in $B12.5@5NP_{BMP2}$, the release occurred more gradually, with 6.12 % and 20.61 % released by days 7 and 14, respectively, and 48.36 % released by the end of 4 weeks (Fig. 7B). For VEGF in V12.5@5NPVEGF, 11.92 % and 26.63 % were released on days 7 and 14, respectively, with 56.6 % released by week 4 (Fig. 7C). These results show that GF release from NP loaded hydrogels occurred more gradually compared to physically entrapped GFs, with release rates of 21.2 %, 13.9 %, and 3.1 % for BMP-2, and 27.4 %, 12.3 %, and 5.7 % for VEGF after 24 h.

Physical entrapment of GFs or the utilization of micro- or NPs as

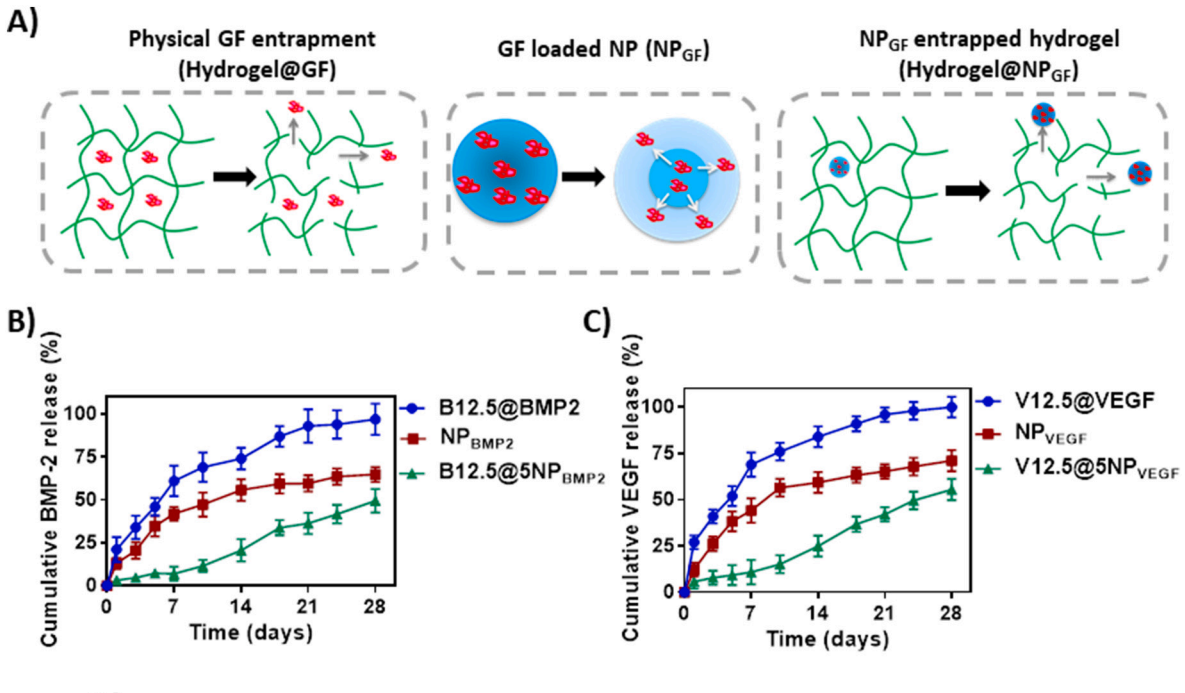

D)

Release kinetic parameters of various formulations

Formulation	Korsmeyer-Peppas	Higuchi	Zero order	First Order	Hixson Crowell
	r^2	r^2	r^2	r^2	r^2
B12.5@BMP2	0.8849	0.9864	0.9548	0.9814	0.9778
NP_{BMP2}	0.9829	0.99	0.8752	0.9391	0.9206
B12.5@5NP_{BMP2}	0.6572	0.8794	0.9852	0.9654	0.9757
V12.5@VEGF	0.7586	0.9938	0.8777	0.9386	0.9201
NP_{VEGF}	0.9829	0.99	0.8752	0.9391	0.9206
V12.5@5NP_{VEGF}	0.6965	0.9147	0.9898	0.9793	0.9867

Fig. 7. GF release profiles from hydrogel scaffolds using different immobilization strategies. (A) Schematic illustration of GF release mechanisms, comparing physical entrapment, NP-mediated loading, and NP-incorporated hydrogel systems. (B) BMP-2 release profiles from: i) Bioink B with physical entrapped BMP-2 (B12.5@BMP2), ii) BMP-2 loaded NPs (NP_{BMP2}), and iii) BMP-2 loaded NP incorporated Bioink B (B12.5@ 5NP_{BMP2}). (C) VEGF release profiles from: i) Bioink V with physical entrapped VEGF (V12.5@VEGF), ii) VEGF loaded NP (NP_{VEGF}), and iii) VEGF loaded NP incorporated Bioink V (V12.5@5NP_{VEGF}). (D) Summary table of release kinetic parameters.

protein reservoirs are common strategies for GF incorporation into scaffolds. However, physical entrapment often results in an uncontrolled burst release followed by degradation-driven release, which can be partially modulated by adjusting the material's degradation rate. In this study, the release of VEGF was faster than BMP-2, which can be attributed to the faster degradation rate and higher swelling of the V12.5 Bioink compared to the B12.5 Bioink. On the other hand, incorporating GF loaded NPs into the hydrogels enabled more precise control over GF release, resulting in long-term, sustained release profiles.

The release kinetics of BMP-2 and VEGF from NP-loaded hydrogels were best described by the Higuchi and Korsmeyer-Peppas models, as shown in Fig. 7D. For the Korsmeyer-Peppas model, the release exponent (n) value > 0.5 indicates "Non-Fickian Diffusion," meaning the release is governed by both diffusion and matrix erosion [80,81]. In addition, the Higuchi model refers to diffusion-controlled release. Here, diffusion is due to the potential gradient of the drug molecule and erosion is due to stress conditions [81,82]. In similar, the Higuchi model was applicable to the release of GFs from physically entrapped hydrogels, where the release is driven by diffusion through the hydrogel pores, which depends on the size and interconnectivity of the pores. For NP-loaded hydrogels, the release profiles best fit the zero-order and Hixson-Crowell models. The zero-order model is particularly useful for drug delivery systems because it delivers the drug at a constant rate over time, making it ideal for long-term, sustained GF release [83]. The Hixson-Crowell model describes release governed by dissolution processes, where the drug release is controlled by changes in the scaffold's surface area and diameter, with less contribution from diffusion [84]. The release from bilayer hydrogel scaffolds loaded with NPs was also zero-order and Hixson Crowell, similar to monolayer scaffolds.

Based on findings of rheological, mechanical, and GF release studies, we conducted in vitro cell culture studies and in vivo studies using NP_{GF} incorporated formulations.

3.3. Cell culture

3.3.1. In vitro cell adhesion studies

To verify our hypothesis and assess the stimulatory effects of GFs (BMP-2 and VEGF) and bioink solutions on cell viability, proliferation

and spreading (OBs and ECs), we conducted a series of cell adhesion studies. As shown in the DAPI-Actin stained images (Fig. 8A and B), both OBs and ECs displayed fully spread morphologies after adhesion to Bioink B (B12.5 or B12.5@5NP_{BMP2}) and Bioink V (V12.5 or V12.5@5NP_{VEGF}). The incorporation of NP_{BMP2} and NP_{VEGF} into the bioinks significantly enhanced cellular spreading compared to the pristine bioinks.

After 7 days of culture, OBs and ECs cultured in hydrogels without NP_{GFs} showed a 5.36-fold and 4.29-fold increase in proliferation, respectively. In contrast, hydrogels containing NP_{GFs} exhibited a 6.11-fold and 5.17-fold increase, highlighting the supportive role of GFs in promoting cellular activity. The metabolic activity and cell proliferation were subsequently assessed using the PrestoBlue assay. Both OBs and ECs demonstrated robust growth and continuous proliferation, with the inclusion of NPBMP2 and NPVEGF leading to significantly higher proliferation rates (Fig. 8C and D). After 7 days of culture, OBs and ECs cultured in hydrogels without NP_{GFs} showed a 5.36 fold and 4.29 fold increases in proliferation, respectively. In contrast, hydrogels containing NP_{GFs} exhibited a 6.11 fold and 5.17 fold increases, highlighting the supportive role of GFs in promoting cellular activity. Additionally, it is well-documented that osteoblast activity increases with the mechanical stiffness of the hydrogel matrix. Consistent with this observation, our results demonstrated an increase in cell proliferation with higher GelMA content in the bioink formulations. These findings emphasize the synergistic effects of GFs and hydrogel properties on cellular behavior, underscoring their potential for advanced tissue engineering applications.

3.3.2. *In vitro cell encapsulation studies*

Following examining cell adhesion behavior on the hydrogel scaffolds, OBs and/or ECs were encapsulated into the monolayer hydrogel scaffolds to evaluate their viability and proliferation. Cell viability was assessed using the Live/Dead assay, revealing high viability for both cell types in all layers post-encapsulation (Fig. 9A, B). These results suggest that the 3D hydrogel structure effectively facilitates nutrient diffusion. Furthermore, the cell counts were notably higher in groups containing NP_{GF} compared to pristine bioinks.

The proliferation of encapsulated OBs and ECs was quantified at days 1, 3, and 7 using the PrestoBlue assay. After 7 days, proliferation of OBs increased 6.13 fold and 6.96 fold within B12.5 and B12.5@5NP_{BMP2} hydrogels, respectively (Fig. 9C). Similarly, ECs exhibited a 7.12 fold and 8.27 fold increases in proliferation in V12.5 and V12.5@5NP_{VEGF} hydrogels, respectively, at day 7. Furthermore, when OBs and ECs were co-cultured in a bilayer hydrogels, proliferation reached 8.39 fold and 6.85 fold increases for hydrogels with and without NP_{GF}, respectively, after 7 days. For all conditions, proliferation gradually increased over time, with a sharp rise at day 3 compared to day 1 ($p < 0.0001$). The enhanced effect of NP_{GF} on proliferation became more pronounced at day 7, consistent with in vitro GF release data.

More importantly, the bilayer hydrogels revealed higher proliferation compared to monolayer scaffolds, attributed to the potential synergistic effect of VEGF and BMP-2, as well as interactions between OBs and ECs. VEGF has been shown to indirectly promote OB differentiation, acting synergistically with BMP-2 [17–19,85]. Our results confirm that the combined use of BMP-2 and VEGF accelerates cellular attachment, growth, and proliferation. To further evaluate cellular morphology, actin filaments were immunofluorescent labeled to examine cells'

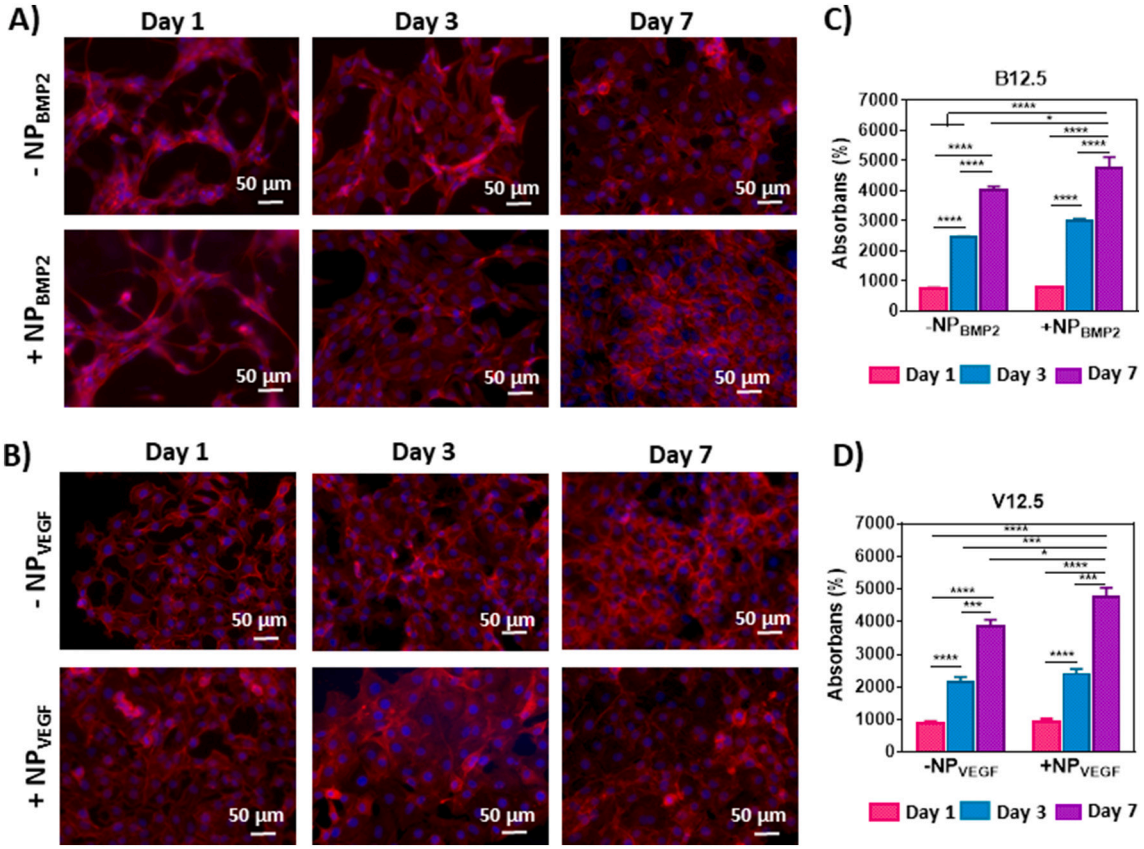

Fig. 8. In vitro cell adhesion and viability on GF-loaded bioinks. (A) Adhesion of OBs on Bioink B (B12.5) and NP_{BMP2} incorporated Bioink B (B12.5@5NP_{BMP2}) at days 1, 3, and 7. (B) Adhesion of ECs on Bioink V (V12.5) and NP_{VEGF} incorporated Bioink V (V12.5@5NP_{VEGF}) at days 1, 3, and 7. (C) PrestoBlue assay results for OBs cultured on Bioink B (B12.5 and B12.5@5NP_{BMP2}) across the same time points. (D) PrestoBlue assay results for ECs cultured on Bioink V (V12.5 and V12.5@5NP_{VEGF}) at days 1, 3, and 7. (ns: $p > 0.05$,*$p < 0.05$, ***$p < 0.001$; ****$p < 0.0001$; One-Way ANOVA, Tukey's Multiple Comparison Test.)

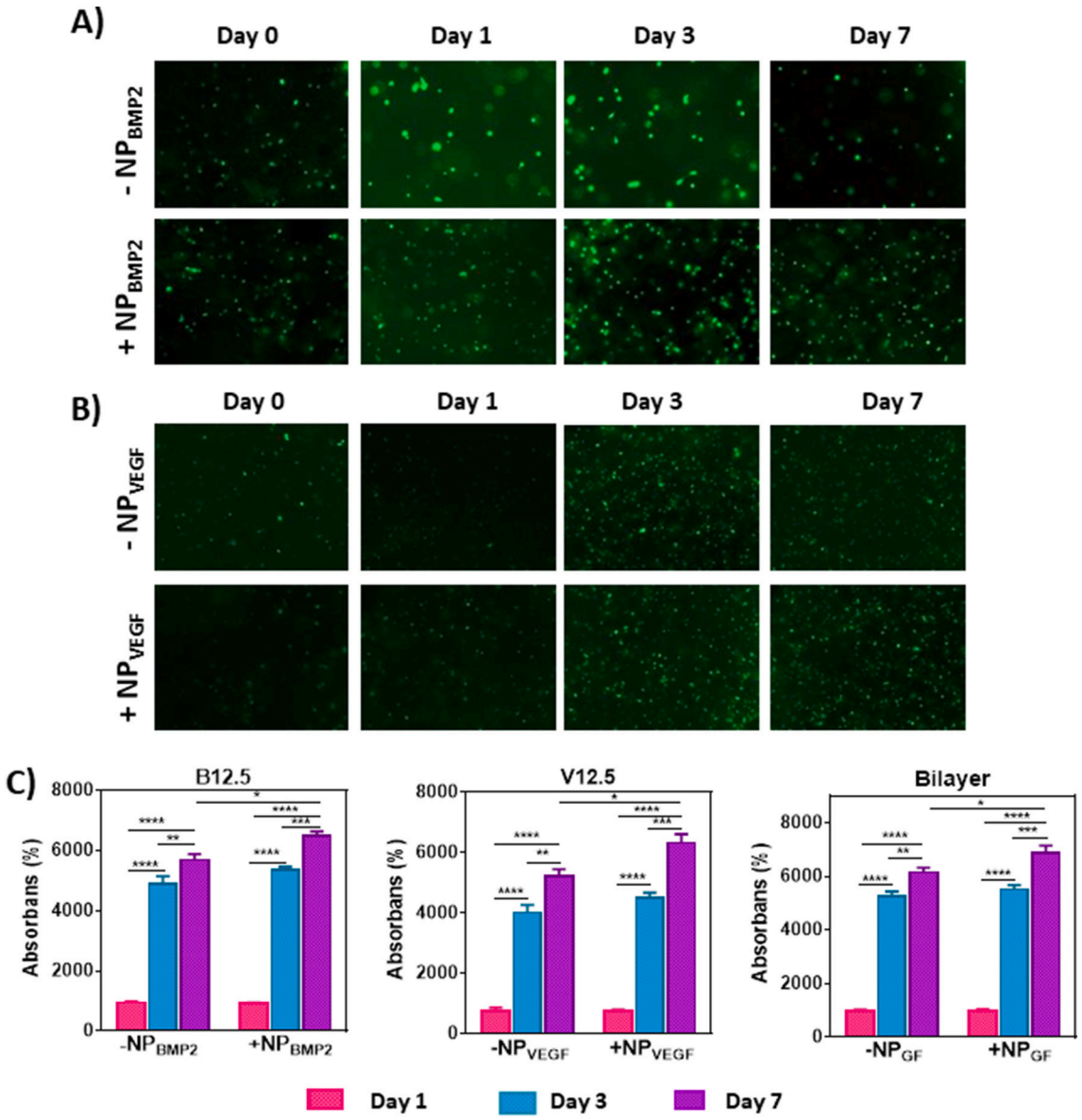

Fig. 9. Live/Dead assay and cell viability of OBs and ECs on NP_{GF} loaded bioinks. (A) Live and dead assay of OBs laden Bioink B (B12.5) and NP_{BMP2} incorporated Bioink B (B12.5@5NP_{BMP2}) at days 1, 3, and 7. (B) Live and dead assay of ECs laden Bioink V (V12.5) and NP_{VEGF} incorporated Bioink V (V12.5@5NP_{VEGF}) at days 1, 3, and 7. (C) The PrestoBlue results for: i) OBs laden Bioink B (B12.5and B12.5@5NP_{BMP2}), ii) ECs laden Bioink V (V12.5 and V12.5@ NP_{VEGF}), and iii) Bilayer hydrogel composed of OBs laden Bioink B and ECs laden Bioink V (B12.5/V12.5 and B12.5@5NP_{BMP2}/V12.5@5NP_{VEGF}) at days 1, 3, and 7. (ns: $p > 0.05$,*p < 0.05, **$p < 0.01$; ***p < 0.001; ****p < 0.000; One-Way ANOVA, Tukey's Multiple Comparison Test.)

skeletal structures in bone mimetic and vascular mimetic hydrogel scaffolds (Fig. 10A and B). Morphological analysis using DAPI and F-actin staining showed that both OBs and ECs initially displayed spherical shapes but adopted a more spread morphology over time. Cells encapsulated in NP_{GF}-containing hydrogels exhibited better spreading compared to those in pristine bioinks. Co-culture conditions in bilayer hydrogels also promoted superior cell spreading.

The cellular features such as mean cell area and cell aspect ratio were calculated to indicate the morphological characteristics of the cells. Cells encapsulated in NP_{GF} embed bioinks exhibited larger cell spreading area than those encapsulated in pristine bioinks (Fig. 10C). Cells encapsulated in NP_{GF} containing bioinks displayed a 1.55-fold and 1.49-fold larger spreading area for OBs and ECs, respectively, compared to pristine bioinks by day 7 ($p > 0.05$). Notably, spreading areas in bilayer hydrogels with NP_{GF} were significantly higher at days 3 ($p < 0.01$) and 7 ($p < 0.0001$) compared to day 1.

3.4. *In vivo studies*

To assess the in vivo regenerative potential of the designed scaffolds, a non-healing critical sized full-thickness defect (5 mm in diameter) was created bilaterally in the calvarial bone in Balb-C mice (Fig. S9). The defects were randomly divided into four experimental groups and filled with V12.5@5NP_{VEGF}, B12.5@5NP_{BMP2}, Bilayer@NP_{GF} (B12.5@5NP_{BMP2}/V12.5@5NP_{VEGF}), or left untreated as a negative control. Bone regeneration was assessed at 8 and 12 weeks post-surgery, with calvarial bones extracted for analysis (Figs. S10 and S11). Histological and immunohistochemical evaluations were performed using H&E, Masson's trichrome, and TB stains and antibodies against COL—I, and OCN at eight and twelve weeks after surgery (Figs. 11 and 12).

Histological results showed no inflammatory cells or tissues in the scaffold-treated groups, confirming the excellent biocompatibility of the scaffolds. In the untreated control group at 8 weeks, the defect areas were predominantly filled with fibrous tissue, with no significant bone

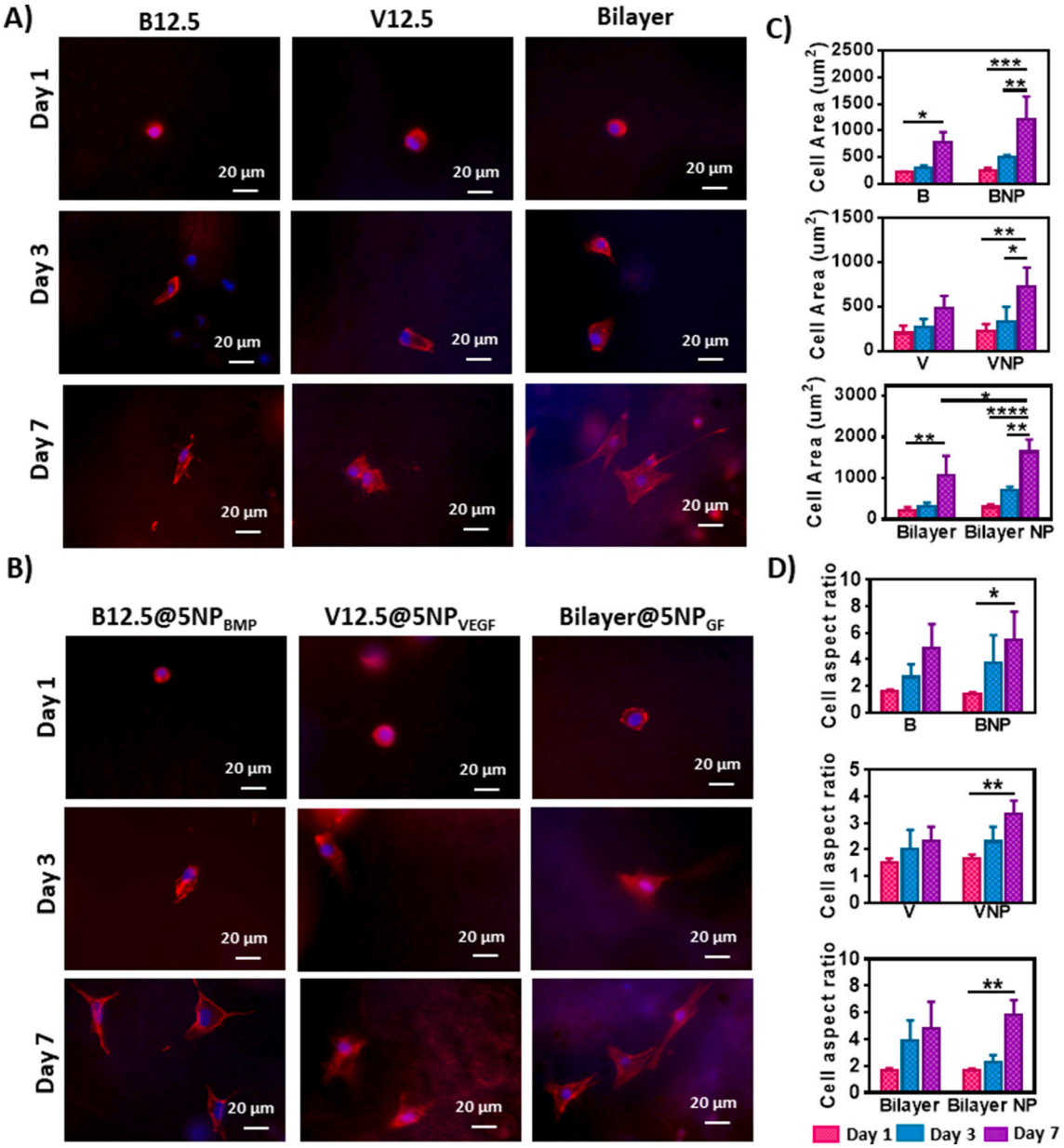

Fig. 10. Rhodamine-Phalloidin and DAPI staining of OBs and ECs laden bioinks. (A) Representative images of i) OBs laden Bioink B (B12.5), ii) ECs laden Bioink V (V12.5), and iii) OBs and ECs laden bilayer hydrogel (B12.5/V12.5) at days 1, 3, and 7. (B) Representative images of i) OBs laden NP_{BMP2} incorporated Bioink B (B12.5@5NP_{BMP2}), ii) ECs laden NP_{VEGF} incorporated Bioink V (V12.5@5NP_{VEGF}), and iii) OBs and ECs laden NP_{GF} incorporated bilayer hydrogel (B12.5@5NP_{BMP2}/V12.5@5NP_{VEGF}) at days 1, 3, and 7. (C) The cell area and (D) The cell aspect ratio (long/short axis) of the i) OBs laden Bioink B (B12.5 and B12.5@5NP_{BMP2}), ii) ECs laden Bioink V (V12.5 and V12.5@5NP_{VEGF}), and iii) bilayer hydrogel composed of OBs laden Bioink B and ECs laden Bioink V (B12.5/V12.5 and B12.5@5NP_{BMP2}/V12.5@5NP_{VEGF}) at days 1, 3 and 7. (ns: $p > 0.05$,*$p < 0.05$, **p < 0.01; ****$p < 0.0001$; One-Way ANOVA, Tukey's Multiple Comparison Test.)

formation or vascularization (Fig. 11). In contrast, the B12.5@5NP_{BMP2} group exhibited newly synthesized bone matrix and enhanced vascularization compared to the control group after 8 weeks ($p < 0.0001$). The V12.5@5NP_{VEGF} and Bilayer@NP_{GF} groups demonstrated significantly higher vascularization scores than B12.5@5NP_{BMP2} (p < 0.0001), with the Bilayer@NP_{GF} group achieving slightly greater vascularization than V12.5@5NP_{VEGF} (p > 0.05). Newly formed small bone trabeculae were detected in the Bilayer@NP_{GF} group, whereas bone formation was absent in the V12.5@5NP_{VEGF} group at 8 weeks. Overall, bone formation scores were highest in the B12.5@5NP_{BMP2} and Bilayer@NP_{GF} groups (p < 0.0001).

At 12 weeks, vascularization increased significantly in the B12.5@5NP_{BMP2} and Bilayer@NP_{GF} groups compared to the 8-week groups ($p < 0.0001$). However, the vascularization of the 12-week V12.5@5NP_{VEGF} was similar to that of the 8-week V12.5@5NP_{VEGF} group ($p > 0.05$) (Fig. S12). Capillary formation in the Bilayer@NP_{GF} group was more extensive than in the V12.5@5NP_{VEGF} and B12.5@5NP_{BMP2} groups (p < 0.0001) (Fig. 12). In the untreated control group, bone formation remained absent at 12 weeks, similar to the 8-week control group (p > 0.05). On the contrary, bone formation significantly increased in all scaffold-treated groups compared to their 8-week counterparts (p < 0.0001) (Fig. S10). 12-week Bilayer@NP_{GF} group exhibited large trabeculae and a well-organized bone matrix surpassing the V12.5@5NP_{VEGF} and B12.5@5NP_{BMP2} group in bone regeneration (p < 0.0001) (Fig. 12).

To assess new bone formation and the expression of proteins indicating osteogenic progression, immunohistochemistry was performed. Immunohistochemical staining for COL-I and OCN revealed higher

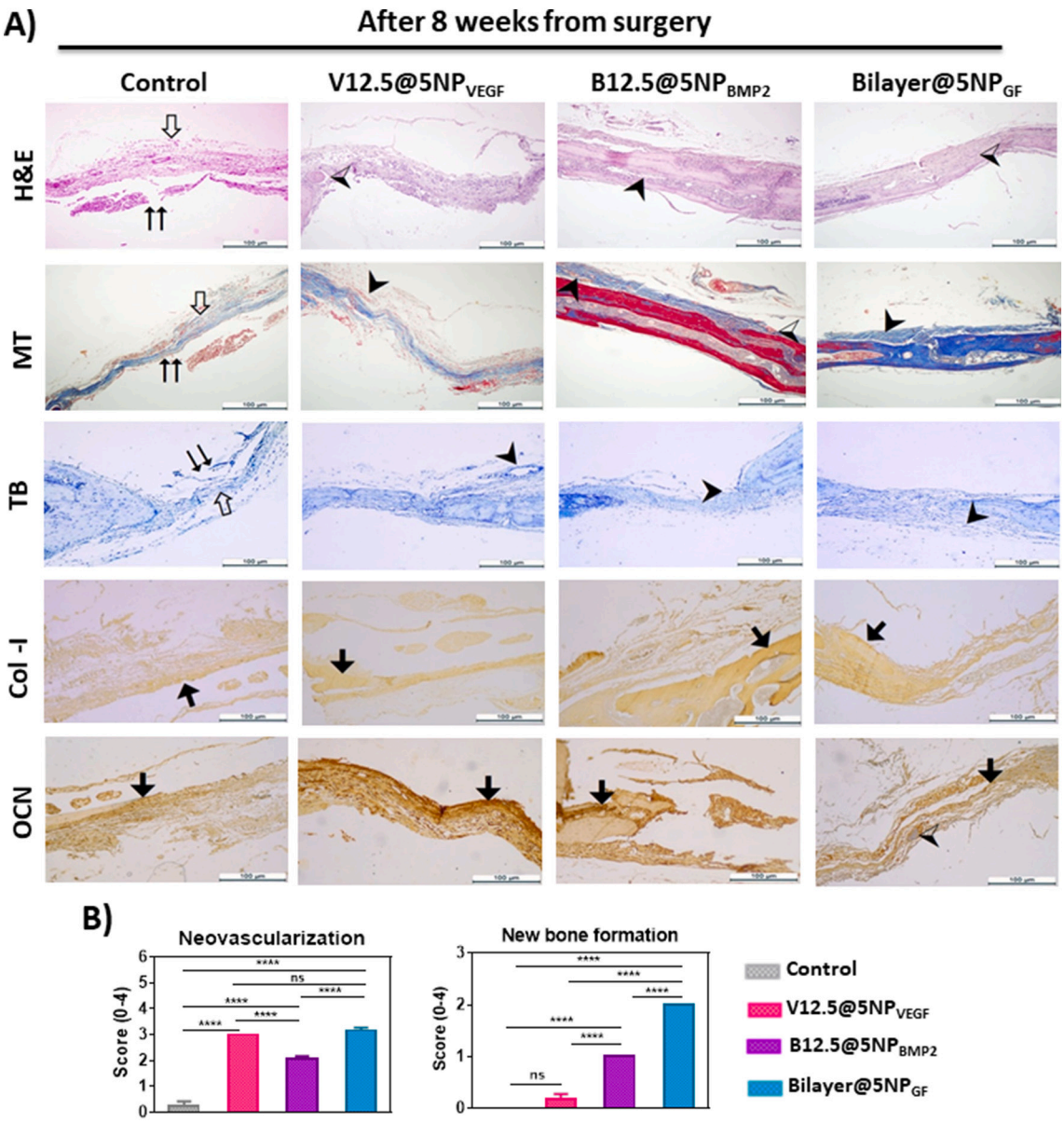

Fig. 11. Histological and immunohistochemical analysis of calvarial tissue sections at 8 weeks post-surgery. (A) Representative photomicrographs of calvarial tissue sections in the experimental groups (control, B12.5@5NP$_{BMP2}$, V12.5@5NP$_{VEGF}$, and bilayer (B12.5@5NP$_{BMP2}$/V12.5@5NP$_{VEGF}$)) stained with H&E, Masson's trichrome, and Toluidine blue stains, and immunostained for COL-I and OCN. Defect region (⇊), fibrous tissue (⇳), vascularization (⮟), bone formation (⮜) and immunopositive areas (⬇) are seen. Scale Bars: 100 μm. (B) Graphs showing the neovascularization and new bone formation score at 8 weeks post-surgery (ns: $p > 0.05$; ****$p < 0.0001$ One-Way ANOVA, Kruskal-Wallis Test.) (For interpretation of the references to colour in this figure legend, the reader is referred to the web version of this article.)

expression levels in scaffold-treated groups compared to controls. COL-I expression was moderate at 8 weeks (Fig. 11) and intense at 12 weeks (Fig. 12) in the B12.5@5NP$_{BMP2}$, V12.5@5NP$_{VEGF}$, and Bilayer@NP$_{GF}$ groups, with the Bilayer@NP$_{GF}$ group showing the strongest immunoreactivity. OCN expression, a late marker of osteoblast maturation, was moderate in the control group but strong in all scaffold-treated groups at both time points. The robust expression of COL-I and OCN in the scaffold-treated groups highlights their ability to promote osteogenic differentiation and extracellular matrix (ECM) formation [86,87]. These findings suggest that all three 3D bioprinted scaffold types effectively support bone regeneration. Among them, the Bilayer@NP$_{GF}$ exhibited superior vascularization, bone formation, and osteogenic differentiation, underscoring its potential as a functional alternative for repairing critical-sized calvarial defects. The combined delivery of BMP-2 and VEGF in the bilayer hydrogel appears to synergistically enhance bone healing, making it a promising strategy for advanced tissue engineering applications.

4. Conclusion

Bone microenvironment is a highly complex and dynamic system where ECM molecules, cells, and GFs interact to modulate new bone formation. The introduction of osteogenic and angiogenic cues, such as cells and GFs, is essential for effective osteogenesis. In particular, controlled release of exogenous GFs such as BMP-2 and VEGF plays a vital role in the success of biomimetic bone scaffolds. NPs with an average size of 147.9 nm (PDI: 0.101) were synthesized using a microfluidic platform, and it is demonstrated that parameters such as flow rate, channel diameter, polymer concentration, and surfactant concentration could effectively control particle size and, consequently, GF

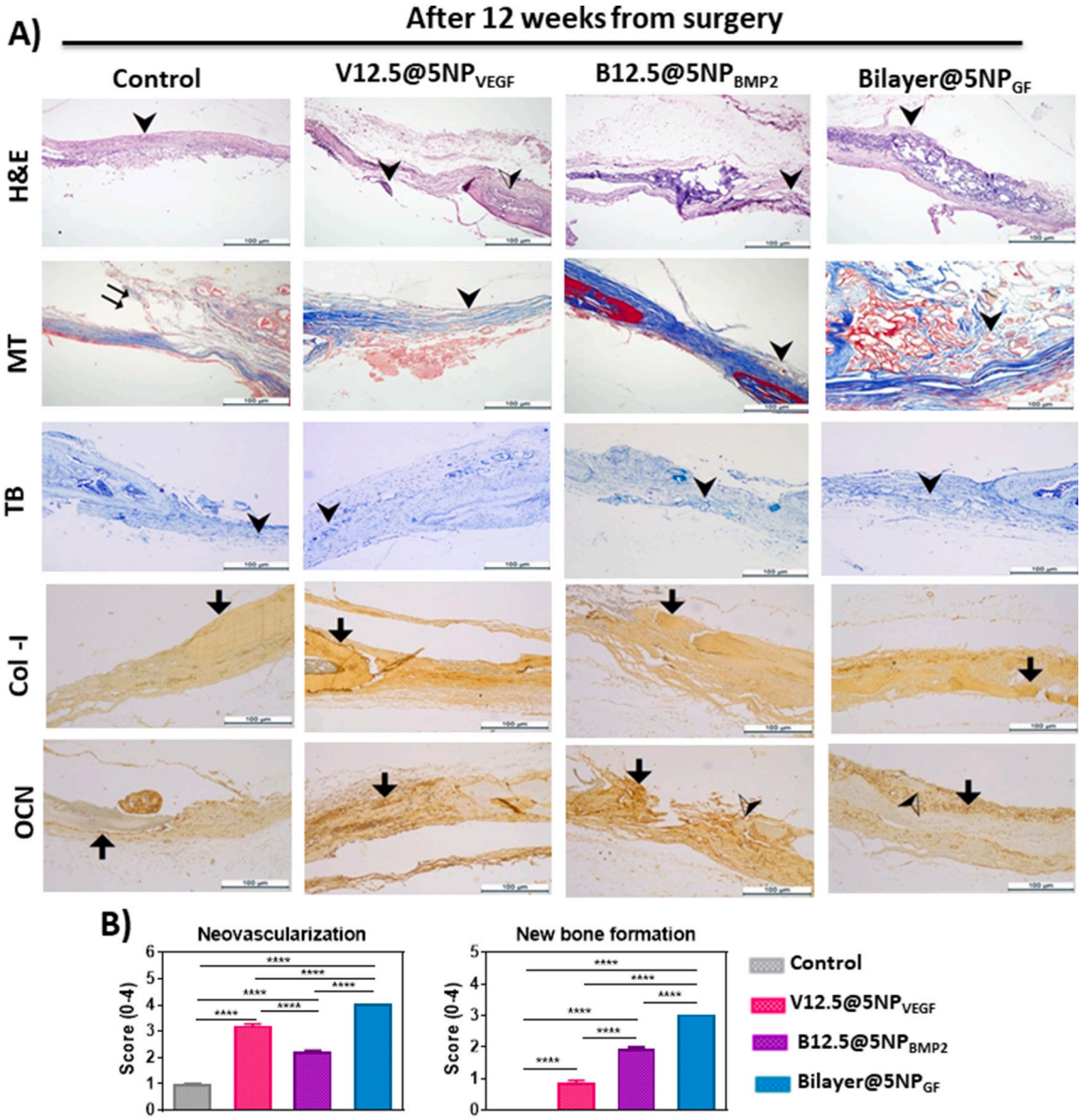

Fig. 12. Histological and immunohistochemical analysis of calvarial tissue sections at 12 weeks post-surgery. (A) Representative photomicrographs of calvarial tissue sections in the experimental groups (control, B12.5@5NP$_{BMP2}$, V12.5@ NP$_{VEGF}$, and B12.5@5NP$_{BMP2}$/V12.5@5NP$_{VEGF}$) stained with H&E, Masson's trichrome, and Toluidine blue stains, and immunostained for COL-I and OCN. Defect region (⇊), vascularization (▾), bone formation (◅) and immunopositive areas (🡻) are seen. Scale Bars: 100 μm. (B) Graphs showing the neovascularization and new bone formation score at 12 weeks post-surgery (****$p < 0.0001$ One-Way ANOVA, Kruskal-Wallis Test.) (For interpretation of the references to colour in this figure legend, the reader is referred to the web version of this article.)

release profiles. Bioink formulations were systematically optimized, and the incorporation of NPs to bioinks enhanced the bioinks' printability, mechanical properties, surface roughness, degradability, and GF release characteristics. In this study, we developed a 3D bioprinted bilayer scaffold with a sequential release of GFs using an extrusion-based dual bioprinter using extrusion based dual bioprinter. The release of BMP-2 or VEGF from single-layer scaffolds promoted significant cellular proliferation. Notably, the dual cytokine release in bilayer scaffolds showed superior cell proliferation and spreading compared to single layer scaffolds. VEGF release amount was particularly effective in the first week, aligning with the natural cascade of bone repair, and maintained beneficial levels over an extended period. In an in vivo calvarial defect model, bilayer scaffolds facilitated superior new bone formation compared to scaffolds containing single GF. This result highlights the importance of synergistic osteoinductive and angiogenic signaling in promoting functional bone regeneration. Taken together, bilayer scaffolds with controlled release of osteogenic and angiogenic factors represent a promising strategy for enhancing bone repair. Their ability to mimic the sequential signaling of natural bone healing makes them a viable option for advancing tissue engineering and regenerative medicine applications.

CRediT authorship contribution statement

Emine Alarcin: Writing – review & editing, Writing – original draft, Supervision, Project administration, Methodology, Investigation, Funding acquisition, Conceptualization. **Zeynep Puren Akguner:** Methodology, Investigation. **Ayca Bal Ozturk:** Writing – review & editing, Methodology, Investigation. **Gokcen Yasayan:** Writing – review & editing, Writing – original draft, Methodology, Investigation. **Esra Ilhan-Ayisigi:** Writing – review & editing, Writing – original draft, Methodology, Investigation, Conceptualization. **Aslihan Kazan:** Writing – review & editing, Methodology, Investigation. **Ozlem Yesil-Celiktas:** Writing – review & editing, Writing – original draft,

Methodology, Investigation. **Dila Sener Akcora:** Methodology, Investigation. **Dilek Akakin:** Writing – review & editing, Writing – original draft, Methodology, Investigation, Conceptualization. **Banu Kocaaga:** Writing – review & editing, Writing – original draft, Methodology, Investigation. **Gamze Eren:** Methodology, Investigation. **Kasım Gunes:** Methodology, Investigation. **Oya Kerimoglu:** Writing – review & editing. **Hatice Kubra Seki:** Methodology, Investigation. **F. Seniha Guner:** Writing – review & editing, Methodology.

Declaration of competing interest

The authors declare that they have no known competing financial interests or personal relationships that could have appeared to influence the work reported in this paper.

Acknowledgments

This study was funded by the Scientific and Technological Research Council of Türkiye (TÜBİTAK) (Grant Number 217S365).

Appendix A. Supplementary data

Supplementary data to this article can be found online at https://doi.org/10.1016/j.ijbiomac.2025.141440.

Data availability

Data will be made available on request.

References

[1] F. Alabdah, A. Alshammari, A. Hidalgo-Bastida, G. Cooper, A review of conventional and novel treatments for osteoporotic hip replacements, Bioengineering 10 (2) (2023) 161, https://doi.org/10.3390/bioengineering10020161.
[2] J.A. Kanis, N. Norton, N.C. Harvey, T. Jacobson, H. Johansson, M. Lorentzon, E. V. McCloskey, C. Willers, F. Borgström, SCOPE 2021: a new scorecard for osteoporosis in Europe, Arch. Osteoporos. 16 (1) (2021) 82, https://doi.org/10.1007/s11657-020-00871-9.
[3] X. Yuan, W. Zhu, Z. Yang, N. He, F. Chen, X. Han, K. Zhou, Recent advances in 3D printing of smart scaffolds for bone tissue engineering and regeneration, Adv. Mater. 36 (34) (2024) 2403641, https://doi.org/10.1002/adma.202403641.
[4] S. Tajvar, A. Hadjizadeh, S.S. Samandari, Scaffold degradation in bone tissue engineering: an overview, Int. Biodeterior. Biodegrad. 180 (2023) 105599, https://doi.org/10.1016/j.ibiod.2023.105599.
[5] V.A. Georgeanu, O. Gingu, I.V. Antoniac, H.O. Manolea, Current options and future perspectives on bone graft and biomaterials substitutes for bone repair, from clinical needs to advanced biomaterials research, Appl. Sci. 13 (14) (2023) 8471, https://doi.org/10.3390/app13148471.
[6] M.P. Ferraz, Bone grafts in dental medicine: an overview of autografts, allografts and synthetic materials, Materials 16 (11) (2023) 4117, https://doi.org/10.3390/ma16114117.
[7] M. Ansari, Bone tissue regeneration: biology, strategies and interface studies, Prog. Biomater. 8 (4) (2019) 223–237, https://doi.org/10.1007/s40204-019-00125-z.
[8] E. Saygili, P. Saglam-Metiner, B. Cakmak, E. Alarcin, G. Beceren, P. Tulum, Y.-W. Kim, K. Gunes, G.G. Eren-Ozcan, D. Akakin, Bilayered laponite/alginate-poly (acrylamide) composite hydrogel for osteochondral injuries enhances macrophage polarization: an in vivo study, Biomater. Adv. (2022) 112721, https://doi.org/10.1016/j.msec.2022.112721.
[9] F. Diomede, G.D. Marconi, L. Fonticoli, J. Pizzicanella, I. Merciaro, P. Bramanti, E. Mazzon, O. Trubiani, Functional relationship between osteogenesis and angiogenesis in tissue regeneration, Int. J. Mol. Sci. 21 (9) (2020) 3242, https://doi.org/10.3390/ijms21093242.
[10] D. Tang, R.S. Tare, L.-Y. Yang, D.F. Williams, K.-L. Ou, R.O.C. Oreffo, Biofabrication of bone tissue: approaches, challenges and translation for bone regeneration, Biomaterials 83 (2016) 363–382, https://doi.org/10.1016/j.biomaterials.2016.01.024.
[11] S. Pina, J.M. Oliveira, R.L. Reis, Natural-based nanocomposites for bone tissue engineering and regenerative medicine: a review, Adv. Mater. 27 (7) (2015) 1143–1169, https://doi.org/10.1002/adma.201403354.
[12] A. Grosso, A. Lunger, M.G. Burger, P.S. Briquez, F. Mai, J.A. Hubbell, D.J. Schaefer, A. Banfi, N. Di Maggio, VEGF dose controls the coupling of angiogenesis and osteogenesis in engineered bone, NPJ Regen. Med. 8 (1) (2023) 15, https://doi.org/10.1038/s41536-023-00288-1.
[13] G. Karima, H.D. Kim, Unlocking the regenerative key: targeting stem cell factors for bone renewal, J. Tissue Eng. 15 (2024) 20417314241287491, https://doi.org/10.1177/20417314241287491.
[14] D. Halloran, H.W. Durbano, A. Nohe, Bone morphogenetic protein-2 in development and bone homeostasis, J. Dev. Biol. 8 (3) (2020) 19, https://doi.org/10.3390/jdb8030019.
[15] J. Qi, H. Wu, G. Liu, Novel strategies for spatiotemporal and controlled bmp-2 delivery in bone tissue engineering, Cell Transplant. 33 (2024) 09636897241276733, https://doi.org/10.1177/09636897241276733.
[16] M. Kang, S. Lee, J.-p. Seo, E.-b. Lee, D. Ahn, J. Shin, Y.-K. Paik, D. Jo, Cell-permeable bone morphogenetic protein 2 facilitates bone regeneration by promoting osteogenesis, Mater. Today Bio. 25 (2024) 100983, https://doi.org/10.1016/j.mtbio.2024.100983.
[17] Y. Bai, Y. Leng, G. Yin, X. Pu, Z. Huang, X. Liao, X. Chen, Y. Yao, Effects of combinations of BMP-2 with FGF-2 and/or VEGF on HUVECs angiogenesis in vitro and CAM angiogenesis in vivo, Cell and Tissue Res. 356 (2014) 109–121, https://doi.org/10.1007/s00441-013-1781-9.
[18] Y. Li, C. Xu, C. Lei, The delivery and activation of growth factors using nanomaterials for bone repair, Pharmaceutics 15 (3) (2023) 1017, https://doi.org/10.3390/pharmaceutics15031017.
[19] G. Shineh, K. Patel, M. Mobaraki, L. Tayebi, Functional approaches in promoting vascularization and angiogenesis in bone critical-sized defects via delivery of cells, growth factors, drugs, and particles, J. Funct. Biomater. 14 (2) (2023) 99, https://doi.org/10.3390/jfb14020099.
[20] X. Chen, B. Tan, Z. Bao, S. Wang, R. Tang, Z. Wang, G. Chen, S. Chen, W.W. Lu, D. Yang, Enhanced bone regeneration via spatiotemporal and controlled delivery of a genetically engineered BMP-2 in a composite hydrogel, Biomaterials 277 (2021) 121117, https://doi.org/10.1016/j.biomaterials.2021.121117.
[21] O. Sipahigil, E. Alarcin, M. Turkoglu, B. Dortunc, H. Karagoz, E. Ulkur, I. Vural, Y. Capan, Characterization, cell proliferation and cytotoxicity evaluation of vascular endothelial growth factor loaded poly (lactic-co-glycolic acid) microspheres, Nobel Med. 8 (1) (2012) 77–82.
[22] T.-M. De Witte, L.E. Fratila-Apachitei, A.A. Zadpoor, N.A. Peppas, Bone tissue engineering via growth factor delivery: from scaffolds to complex matrices, Regen. Biomater. 5 (4) (2018) 197–211, https://doi.org/10.1093/rb/rby013.
[23] M. Yu, A. Mathew, D. Liu, Y. Chen, J. Wu, Y. Zhang, N. Zhang, Microfluidics for formulation and scale-up production of nanoparticles for biopharma industry, in: Microfluidics in Pharmaceutical Sciences: Formulation, Drug Delivery, Screening, and Diagnostics, Springer, 2024, pp. 395–420.
[24] S. Gimondi, H. Ferreira, R.L. Reis, N.M. Neves, Microfluidic devices: a tool for nanoparticle synthesis and performance evaluation, ACS Nano 17 (15) (2023) 14205–14228, https://doi.org/10.1021/acsnano.3c01117.
[25] M.C. Operti, A. Bernhardt, S. Grimm, A. Engel, C.G. Figdor, O. Tagit, PLGA-based nanomedicines manufacturing: technologies overview and challenges in industrial scale-up, Int. J. Pharm. 605 (2021) 120807, https://doi.org/10.1016/j.ijpharm.2021.120807.
[26] N. Raveendran, S. Ivanovski, C. Vaquette, The effect of culture conditions on the bone regeneration potential of osteoblast-laden 3D bioprinted constructs, Acta Biomater. 156 (2023) 190–201, https://doi.org/10.1016/j.actbio.2022.09.042.
[27] J. Kim, H.S. Choi, Y.M. Kim, S.C. Song, Thermo-responsive nanocomposite bioink with growth-factor holding and its application to bone regeneration, Small 19 (9) (2023) 2203464, https://doi.org/10.1002/smll.202203464.
[28] M. Shahrezaie, A. Zamanian, M. Sahranavard, M.H. Shahrezaee, A critical review on the 3D bioprinting in large bone defects regeneration, Bioprinting (2023) e00327, https://doi.org/10.1016/j.bprint.2023.e00327.
[29] E. Alarçin, B. İzbudak, E. Yüce Erarslan, S. Domingo, R. Tutar, K. Titi, B. Kocaaga, F.S. Guner, A. Bal-Öztürk, Optimization of methacrylated gelatin/layered double hydroxides nanocomposite cell-laden hydrogel bioinks with high printability for 3D extrusion bioprinting, J. Biomed. Mater. Res. A 111 (2) (2023) 209–223, https://doi.org/10.1002/jbm.a.37450.
[30] Z. Fu, N. Hai, Y. Zhong, W. Sun, Printing GelMA bioinks: a strategy for building in vitro model to study nanoparticle-based minocycline release and cellular protection under oxidative stress, Biofabrication 16 (2) (2024) 025040, https://doi.org/10.1088/1758-5090/ad30c3.
[31] S. Asim, T.A. Tabish, U. Liaqat, I.T. Ozbolat, M. Rizwan, Advances in gelatin bioinks to optimize bioprinted cell functions, Adv. Healthc. Mater. 12 (17) (2023) 2203148, https://doi.org/10.1002/adhm.202203148.
[32] Z. Galliger, C.D. Vogt, H.R. Helms, A. Panoskaltsis-Mortari, Extracellular matrix microparticles improve GelMA bioink resolution for 3D bioprinting at ambient temperature, Macromol. Mater. Eng. 307 (10) (2022) 2200196, https://doi.org/10.1002/mame.202200196.
[33] B. Zhou, X. Jiang, X. Zhou, W. Tan, H. Luo, S. Lei, Y. Yang, GelMA-based bioactive hydrogel scaffolds with multiple bone defect repair functions: therapeutic strategies and recent advances, Biomater. Res. 27 (1) (2023) 86, https://doi.org/10.1186/s40824-023-00422-6.
[34] D. Chimene, L. Miller, L.M. Cross, M.K. Jaiswal, I. Singh, A.K. Gaharwar, Nanoengineered osteoinductive bioink for 3D bioprinting bone tissue, ACS Appl. Mater. Interfaces 12 (14) (2020) 15976–15988, https://doi.org/10.1021/acsami.9b19037.
[35] H. Rastin, R.T. Ormsby, G.J. Atkins, D. Losic, 3D bioprinting of methylcellulose/gelatin-methacryloyl (MC/GelMA) bioink with high shape integrity, ACS Appl. Bio Mater. 3 (3) (2020) 1815–1826, https://doi.org/10.1021/acsabm.0c00169.
[36] L. Yang, L. Fan, X. Lin, Y. Yu, Y. Zhao, Pearl powder hybrid bioactive scaffolds from microfluidic 3D printing for bone regeneration, Adv. Sci. 10 (34) (2023) 2304190, https://doi.org/10.1002/advs.202304190.
[37] L. Yang, W. Yang, W. Xu, Y. Zhao, L. Shang, Bio-inspired Janus microcarriers with sequential actives release for bone regeneration, J. Chem. Eng. 476 (2023) 146797, https://doi.org/10.1016/j.cej.2023.146797.

[38] H.S. Hwang, C.-S. Lee, Recent progress in hyaluronic-acid-based hydrogels for bone tissue engineering, Gels 9 (7) (2023) 588, https://doi.org/10.3390/gels9070588.
[39] X. Cui, C. Huang, Z. Chen, M. Zhang, C. Liu, K. Su, J. Wang, L. Li, R. Wang, B. Li, Hyaluronic acid facilitates bone repair effects of calcium phosphate cement by accelerating osteogenic expression, Bioact. Mater. 6 (11) (2021) 3801–3811, https://doi.org/10.1016/j.bioactmat.2021.03.028.
[40] M. Bramosanti, L. Chronopoulou, F. Grillo, A. Valletta, C. Palocci, Microfluidic-assisted nanoprecipitation of antiviral-loaded polymeric nanoparticles, Colloids Surf. A Physicochem. Eng. Asp. (2017), https://doi.org/10.1016/j.colsurfa.2017.04.062.
[41] E. Saygili, E. Kaya, E. Ilhan-Ayisigi, P. Saglam-Metiner, E. Alarcin, A. Kazan, E. Girgic, Y.-W. Kim, K. Gunes, G.G. Eren-Ozcan, An alginate-poly (acrylamide) hydrogel with TGF-β3 loaded nanoparticles for cartilage repair: biodegradability, biocompatibility and protein adsorption, Int. J. Biol. Macromol. 172 (2021) 381–393, https://doi.org/10.1016/j.ijbiomac.2021.01.069.
[42] E. Alarçin, A.B. Dokgöz, Z.P. Akgüner, H.K. Seki, A. Bal-Öztürk, Gelatin methacryloyl/nanosilicate nanocomposite hydrogels encapsulating dexamethasone with a tunable crosslinking density for bone repair, J. Drug Deliv. Technol. 77 (2022) 103844, https://doi.org/10.1016/j.jddst.2022.103844.
[43] C.G. England, M.C. Miller, A. Kuttan, J.O. Trent, H.B. Frieboes, Release kinetics of paclitaxel and cisplatin from two and three layered gold nanoparticles, Eur. J. Pharm. Biopharm. 92 (2015) 120–129, https://doi.org/10.1016/j.ejpb.2015.02.017.
[44] J. Li, Q. Xu, B. Teng, C. Yu, L. Song, Y.-X. Lai, J. Zhang, W. Zheng, P.-G. Ren, Investigation of angiogenesis in bioactive 3-dimensional poly (d, l-lactide-co-glycolide)/nano-hydroxyapatite scaffolds by in vivo multiphoton microscopy in murine calvarial critical bone defect, Acta Biomater. 42 (2016) 389–399, https://doi.org/10.1016/j.actbio.2016.06.024.
[45] Y.W. Chen, M.Y. Chen, D.J. Hsieh, S. Periasamy, K.C. Yen, C.T. Chuang, H.C. Wang, F.W. Tseng, J.C. Kuo, H.H. Chien, Evaluating the bone-regenerative role of the decellularized porcine bone xenograft in a canine extraction socket model, Clin Exp Dent Res. 7 (4) (2021) 409–418, https://doi.org/10.1002/cre2.361.
[46] M. Khadra, N. Kasem, H.R. Haanæs, J.E. Ellingsen, S.P. Lyngstadaas, Enhancement of bone formation in rat calvarial bone defects using low-level laser therapy, Oral Surg. Oral Med. Oral Pathol. Oral Radiol. Endod. 97 (6) (2004) 693–700, https://doi.org/10.1016/j.tripleo.2003.11.008.
[47] E.C. Jensen, Quantitative analysis of histological staining and fluorescence using ImageJ, The Ana. Rec. 296 (3) (2013) 378–381, https://doi.org/10.1002/ar.22641.
[48] A. Kazan, O. Yesil-Celiktas, Y.S. Zhang, Fabrication of thymoquinone-loaded albumin nanoparticles by microfluidic particle synthesis and their effect on planarian regeneration, Macromol. Biosci. 19 (11) (2019) 1900182, https://doi.org/10.1002/mabi.201900182.
[49] R. Zoqlam, C.J. Morris, M. Akbar, A.M. Alkilany, S.I. Hamdallah, P. Belton, S. Qi, Evaluation of the benefits of microfluidic-assisted preparation of polymeric nanoparticles for DNA delivery, Mater. Sci. Eng. C Mater. Biol. Appl. 127 (2021) 112243, https://doi.org/10.1016/j.msec.2021.112243.
[50] Y. Liu, G. Yang, Y. Hui, S. Ranaweera, C.X. Zhao, Microfluidic nanoparticles for drug delivery, Small 18 (36) (2022) 2106580, https://doi.org/10.1002/smll.202106580.
[51] S.I. Hamdallah, R. Zoqlam, P. Erfle, M. Blyth, A.M. Alkilany, A. Dietzel, S. Qi, Microfluidics for pharmaceutical nanoparticle fabrication: the truth and the myth, Int. J. Pharm. 584 (2020) 119408, https://doi.org/10.1016/j.ijpharm.2020.119408.
[52] F. Sharifi, O. Yesil-Celiktas, A. Kazan, S. Maharjan, S. Saghazadeh, K. Firoozbakhsh, B. Firoozabadi, Y.S. Zhang, A hepatocellular carcinoma–bone metastasis-on-a-chip model for studying thymoquinone-loaded anticancer nanoparticles, Bio-Des. Manuf. 3 (2020) 189–202, https://doi.org/10.1007/s42242-020-00074-8.
[53] R.M. Gebreel, M.M. Abdellatif, A. Attia, Lomefloxacin-loaded PLGA hollow nanospheres for healing MRSA-infected diabetic wound; optimization, in vitro and in vivo studies, J. Drug Deliv. Technol. 100 (2024) 106050, https://doi.org/10.1016/j.jddst.2024.106050.
[54] A. Kazan, C. Sevimli-Gur, O. Yesil-Celiktas, N.T. Dunford, In vitro tumor suppression properties of blueberry extracts in liquid and encapsulated forms, Eur. Food Res. Technol. 243 (6) (2017) 1057–1063, https://doi.org/10.1007/s00217-016-2819-5.
[55] K.R. Mamaghani, S.M. Naghib, A. Zahedi, M. Mozafari, Synthesis and microstructural characterization of GelMa/PEGDA hybrid hydrogel containing graphene oxide for biomedical purposes, Mater. Today: Proc. 5 (7) (2018) 15635–15644, https://doi.org/10.1016/j.matpr.2018.04.173.
[56] T.D. Usal, D. Yucel, V. Hasirci, A novel GelMA-pHEMA hydrogel nerve guide for the treatment of peripheral nerve damages, Int. J. Biol. Macromol. 121 (2019) 699–706, https://doi.org/10.1016/j.ijbiomac.2018.10.060.
[57] W. Liu, M.A. Heinrich, Y. Zhou, A. Akpek, N. Hu, X. Liu, X. Guan, Z. Zhong, X. Jin, A. Khademhosseini, Extrusion bioprinting of shear-thinning gelatin methacryloyl bioinks, Adv. Healthc. Mater. 6 (12) (2017) 1601451, https://doi.org/10.1002/adhm.201601451.
[58] W. Liu, Y.S. Zhang, M.A. Heinrich, F. De Ferrari, H.L. Jang, S.M. Bakht, M. M. Alvarez, J. Yang, Y.C. Li, G. Trujillo-de Santiago, Rapid continuous multimaterial extrusion bioprinting, Adv. Mater. 29 (3) (2017), https://doi.org/10.1002/adma.201604630.
[59] G. Yaşayan, E. Alarçin, A. Bal-Öztürk, M. Avci-Adali, Natural polymers for wound dressing applications, Stud. Nat. Prod. Chem. 74 (2022) 367–441.
[60] J. Karvinen, M. Kellomäki, 3D-bioprinting of self-healing hydrogels, Eur. Polym. J. (2024) 112864, https://doi.org/10.1016/j.eurpolymj.2024.112864.
[61] T. Gao, G.J. Gillispie, J.S. Copus, A.K. Pr, Y.-J. Seol, A. Atala, J.J. Yoo, S.J. Lee, Optimization of gelatin–alginate composite bioink printability using rheological parameters: a systematic approach, Biofabrication 10 (3) (2018) 034106, https://doi.org/10.1088/1758-5090/aacdc7.
[62] A. Indurkar, P. Bangde, M. Gore, P. Reddy, R. Jain, P. Dandekar, Optimization of guar gum-gelatin bioink for 3D printing of mammalian cells, Bioprinting 20 (2020) e00101, https://doi.org/10.1016/j.bprint.2020.e00101.
[63] L.Y. Zhou, J. Fu, Y. He, A review of 3D printing technologies for soft polymer materials, Adv. Funct. Mater. 30 (28) (2020) 2000187, https://doi.org/10.1002/adfm.202000187.
[64] S. Uman, A. Dhand, J.A. Burdick, Recent advances in shear-thinning and self-healing hydrogels for biomedical applications, J. Appl. Polym. Sci. 137 (25) (2020) 48668, https://doi.org/10.1002/app.48668.
[65] N.D. Sanandiya, J. Vasudevan, R. Das, C.T. Lim, J.G. Fernandez, Stimuli-responsive injectable cellulose thixogel for cell encapsulation, Int. J. Biol. Macromol. 130 (2019) 1009–1017, https://doi.org/10.1016/j.ijbiomac.2019.02.135.
[66] Q. Liu, J. Yang, Y. Wang, T. Wu, Y. Liang, K. Deng, G. Luan, Y. Chen, Z. Huang, K. Yue, Direct 3D bioprinting of tough and antifatigue cell-laden constructs enabled by a self-healing hydrogel bioink, Biomacromolecules 24 (6) (2023) 2549–2562, https://doi.org/10.1021/acs.biomac.3c00057.
[67] H. Daemi, M. Barikani, Synthesis and characterization of calcium alginate nanoparticles, sodium homopolymannuronate salt and its calcium nanoparticles, Sci. Iran. 19 (6) (2012) 2023–2028, https://doi.org/10.1016/j.scient.2012.10.005.
[68] J. Carneiro, P.M. Döll-Boscardin, B.C. Fiorin, J.M. Nadal, P.V. Farago, J.P.D. Paula, Development and characterization of hyaluronic acid-lysine nanoparticles with potential as innovative dermal filling, Braz. J. Pharm. Sci. 52 (4) (2016) 645–651, https://doi.org/10.1590/S1984-82502016000400008.
[69] A. Assmann, A. Vegh, M. Ghasemi-Rad, S. Bagherifard, G. Cheng, E.S. Sani, G. U. Ruiz-Esparza, I. Noshadi, A.D. Lassaletta, S. Gangadharan, A. Tamayol, A. Khademhosseini, N. Annabi, A highly adhesive and naturally derived sealant, Biomaterials 140 (2017) 115–127, https://doi.org/10.1016/j.biomaterials.2017.06.004.
[70] V.B.V. Maciel, C.M.P. Yoshida, T.T. Franco, Chitosan/pectin polyelectrolyte complex as a pH indicator, Carbohydr. Polym. 132 (2015) 537–545, https://doi.org/10.1016/j.carbpol.2015.06.047.
[71] J. Na, C. Tai, Z. Wang, Z. Yang, X. Chen, J. Zhang, L. Zheng, Y. Fan, Stiff extracellular matrix drives the differentiation of mesenchymal stem cells toward osteogenesis by the multiscale 3D genome reorganization, Biomaterials 312 (2025) 122715, https://doi.org/10.1016/j.biomaterials.2024.122715.
[72] L. Cheng, H. Yue, H. Zhang, Q. Liu, L. Du, X. Liu, J. Xie, Y. Shen, The influence of microenvironment stiffness on endothelial cell fate: implication for occurrence and progression of atherosclerosis, Life Sci. (2023) 122233, https://doi.org/10.1016/j.lfs.2023.122233.
[73] J.A. Wood, N.M. Shah, C.T. McKee, M.L. Hughbanks, S.J. Liliensiek, P. Russell, C. J. Murphy, The role of substratum compliance of hydrogels on vascular endothelial cell behavior, Biomaterials 32 (22) (2011) 5056–5064, https://doi.org/10.1016/j.biomaterials.2011.03.054.
[74] L. Santos, G. Fuhrmann, M. Juenet, N. Amdursky, C.M. Horejs, P. Campagnolo, M. M. Stevens, Extracellular stiffness modulates the expression of functional proteins and growth factors in endothelial cells, Adv. Healthc. Mater. 4 (14) (2015) 2056–2063, https://doi.org/10.1002/adhm.201500338.
[75] C.-S. Lee, H.S. Hwang, Starch-based hydrogels as a drug delivery system in biomedical applications, Gels 9 (12) (2023) 951, https://doi.org/10.3390/gels9120951.
[76] S. Sethi, P. Mahajan, S. Thakur, N. Sharma, N. Singh, A. Kumar, A. Kaur, B.S. Kaith, Design and evaluation of fluorescent chitosan-starch hydrogel for drug delivery and sensing applications, Int. J. Biol. Macromol. 274 (2024) 133486, https://doi.org/10.1016/j.ijbiomac.2024.133486.
[77] A. Zhang, L. Sun, K. Chen, C. Liu, Y. Yuan, 3D printing viscoelastic hydrogel-based scaffolds with a swelling-dependent gate for cartilage injury regeneration, J. Chem. Eng. 480 (2024) 147260, https://doi.org/10.1016/j.cej.2023.147260.
[78] Q. Wang, Y. Zhang, B. Li, L. Chen, Controlled dual delivery of low doses of BMP-2 and VEGF in a silk fibroin–nanohydroxyapatite scaffold for vascularized bone regeneration, J. Mater. Chem. B 5 (33) (2017) 6963–6972, https://doi.org/10.1039/C7TB00949F.
[79] E. Alarcin, C. Demirbag, S. Karsli-Ceppioglu, O. Kerimoglu, A. Bal-Ozturk, Development and characterization of oxaceprol-loaded poly-lactide-co-glycolide nanoparticles for the treatment of osteoarthritis, Drug Dev. Res. (2020), https://doi.org/10.1002/ddr.21642.
[80] R.W. Korsmeyer, R. Gurny, E. Doelker, P. Buri, N.A. Peppas, Mechanisms of solute release from porous hydrophilic polymers, Int. J. Pharm. 15 (1) (1983) 25–35, https://doi.org/10.1016/0378-5173(83)90064-9.
[81] M. Askarizadeh, N. Esfandiari, B. Honarvar, S.A. Sajadian, A. Azdarpour, Kinetic modeling to explain the release of medicine from drug delivery systems, ChemBioEng Rev. 10 (6) (2023) 1006–1049, https://doi.org/10.1002/cben.202300027.
[82] T. Higuchi, Mechanism of sustained-action medication. Theoretical analysis of rate of release of solid drugs dispersed in solid matrices, J. Pharm. Sci. 52 (12) (1963) 1145–1149, https://doi.org/10.1002/jps.2600521210.
[83] M.-L. Laracuente, H.Y. Marina, K.J. McHugh, Zero-order drug delivery: state of the art and future prospects, J. Control. Release 327 (2020) 834–856, https://doi.org/10.1016/j.jconrel.2020.09.020.
[84] A.-M. Craciun, M.L. Barhalescu, M. Agop, L. Ochiuz, Theoretical modeling of long-time drug release from nitrosalicyl-imine-chitosan hydrogels through multifractal logistic type laws, Comput. Math. Methods Med. 2019 (2019), https://doi.org/10.1155/2019/4091464.

[85] H.-X. Zhang, X.-P. Zhang, G.-Y. Xiao, Y. Hou, L. Cheng, M. Si, S.-S. Wang, Y.-H. Li, L. Nie, In vitro and in vivo evaluation of calcium phosphate composite scaffolds containing BMP-VEGF loaded PLGA microspheres for the treatment of avascular necrosis of the femoral head, Mater. Sci. Eng. C 60 (2016) 298–307, https://doi.org/10.1016/j.msec.2015.11.055.

[86] S. Gao, B. Chen, M. Gao, Y. Xu, X. Yang, C. Yang, S. Pan, Substrate stiffness of bone microenvironment controls functions of pre-osteoblasts and fibroblasts in vitro, Biomimetics 8 (4) (2023) 344, https://doi.org/10.3390/biomimetics8040344.

[87] M. Wu, M. Qin, X. Wang, Therapeutic effects of isoquercetin on ovariectomy-induced osteoporosis in mice, Nat. Prod. Bioprospect. 13 (1) (2023) 20, https://doi.org/10.1007/s13659-023-00383-2.